MARC ANALYSIS RESEARCH CORP.
105 Medway Street
Providence, Rhode Island 02906
Tel. 401/751-9120

Report TR73-7 for the

National Aeronautics and

Space Administration

on

WATER IMPACT ANALYSIS OF SPACE SHUTTLE SOLID ROCKET MOTOR BY THE FINITE ELEMENT METHOD

by

O. Buyukozturk, H.D. Hibbitt, E.P. Sorensen
Marc Analysis Research Corporation
Providence, Rhode Island 02906

March, 1974

Final report on Contract No. NAS8-29195 with National Aeronautics and Space Adminstration, Marshall Space Flight Center, Alabama 35812

TABLE OF CONTENTS

ABSTRACT

A study was made of the Space Shuttle Rocket Motor Casing during water impact. The problem was assumed to be static and equivalent static loads were used. The objective was to ascertain that current finite element analysis techniques could be relied on for design purposes.

Preliminary analysis showed that the doubly curved triangular shell elements were too stiff for these shell structures. The doubly curved quadrilateral shell elements were found to give much improved results.

A total of six load cases were analyzed in this study. The load cases were either those resulting from a static test using reaction straps to simulate the drop conditions or under assumed hydrodynamic conditions resulting from a drop test. The latter hydrodynamic conditions were obtained through an emperical fit of available data.

Results obtained from a linear analysis were found to be consistent with results obtained elsewhere with NASTRAN and BOSOR.

The nonlinear analysis showed that the originally assumed loads would result in failure of the shell structures. The nonlinear analysis also showed that it was useful to apply internal pressure as a stabilizing influence on collapse.

A final analysis with an updated estimate of load conditions resulted in linear behavior up to full load.

In this report we describe the analysis of the Space Shuttle Rocket Motor Casing. The analysis was performed by the finite element method and use was made of doubly curved shell elements. The MARC-CDC program was used in this analysis. This program is described in the Appendix.

The object of the analysis was to verify the use of such analysis by comparing its results with experiment. A further point of interest was to determine if the structure would behave linearly up to full load. The shell structure is loaded, in practice, by inertia loads. A technique was developed during the study to account for the pseudo-static loads and reactions due to inertia.

The analysis is divided into four parts:

(a) In the initial stage the structure was modelled by means of triangular shell elements. These were found to give too stiff a result. (Sections 2 and 3)

(b) Subsequently, a convergence study was made to compare the triangular shell element with the quadrilateral shell element. The quadrilateral element was found to be a much better element for this type of geometry and loading (Section 4).

(c) The quadrilateral element was then used for analysis of the static model and the drop test model in the linear and nonlinear regime. (Sections 5 and 6)

(d) Finally, a new estimate of the actual load during a drop test was used for an incremental analysis. (Section 7)

Idealization

The static test model consists of a cylinder with two spherical closures at the ends. The model is shown in Figure 2.1. In the finite element idealization 238 shell elements were used with a total of 160 nodes (Fig. 2.2). Appropriate boundary conditions were imposed to account for symmetry and remove rigid body motion. Analysis assumptions are discussed in the following sections.

Thickness

The assumed uniform thickness for the cylinder and the spheres are 0.347" and 0.231" respectively. These thicknesses are based on the mean values employed in constructing actual experimental models. The stiffening effect at the joints is taken into account only at the end areas of the cylinder as shown in Figure 2.1. In these areas the shell elements are uniformly thickened consistent with the cross-sectional area of the joints. Uniform thickness of 0.444" and 0.534" are used corresponding to fwd and aft end joint areas respectively.

It is noted that a beam-shell model was initially generated to simulate the stiffening effect. However, this model was abondoned because of the cost involved in the analysis of that model.

Boundary Conditions

Since the structure and loading are symmetrical with respect to the xz plane (Figure 2.1), the following boundary conditions are imposed. For all nodes on the xz plane:

$$v = 0, \quad \frac{\partial v}{\partial \theta_2} = 0, \quad \frac{\partial u}{\partial \theta_1} = 0, \quad \frac{\partial w}{\partial \theta_1} = 0$$

In addition to the symmetry conditions the following boundary conditions are imposed to prevent rigid body motion:

At Node A:

$$u = 0 \text{ and } w = 0$$

At Node B:

$$u = 0$$

Note that these latter conditions should impose no loads.

Loading

The assumed loading for the present analysis is shown in Figure 2.3, and is defined as follows in terms of the surface coordinates θ^1 (=Rx) and θ^2 (=z). The pressure is varied linearly along the half length of the cylinder. Following the notation defined in Figure 2.3, the variation of peak section pressure P along the length (at $\theta^1 = 0$) is:

$$P = \frac{P_b - P_a}{\theta_b^2 - \theta_a^2} (\theta^2 - \theta_a^2) + P_a \qquad (1)$$

The pressure is varied also along the circumference as a cosine function so that the pressure vanishes at $\bar{\theta}^1$, where $\bar{\theta}^1$ is defined as a linear function of θ^2:

$$\bar{\theta}^1 = \frac{\bar{\theta}_b^1 - \bar{\theta}_a^1}{\theta_b^2 - \theta_a^2} (\theta^2 - \theta_a^2) + \bar{\theta}_a^1 \qquad (2)$$

Therefore, the pressure p at a general point (θ^1, θ^2) is given by following expression:

$$P(\theta^1, \theta^2) = \left[\frac{P_b - P_a}{\theta_b^2 - \theta_a^2}(\theta^2 - \theta_a^2) + P_a\right] \cdot \cos\left[\frac{\pi}{2}\left(\frac{\theta^1}{\frac{\bar{\theta}_b^1 - \bar{\theta}_a^1}{\theta_b^2 - \theta_a^2}(\theta^2 - \theta_a^2) + \bar{\theta}_a^1}\right)\right] \qquad (3)$$

The numerical values assumed for the present analysis are:

$P_a = 45.$ psi

$P_b = 8.$ psi

} Peak values of pressure on symmetry plane

$\bar{\alpha}_a^1 = 15°$ $(\bar{\theta}_a^1 = \bar{\alpha}_b^1 \cdot R)$

$\bar{\alpha}_b^1 = 60°$ $(\bar{\theta}_b^1 = \bar{\alpha}_b^1 \cdot R)$

} circumferential extents of pressure loading

The experimental strap support system was assumed to be frictionless, so that it provides a uniform normal pressure over the entire strap angle (120° - 60° in the symmetric half model). Then this reactive pressure, p_r as seen in Figure 2.4, was computed as a function of axial position (θ^2) to provide section equilibrium in the x-direction, on the assumption that this was a reasonable modelling of the experimental procedure.

Section equilibrium is achieved as follows:

The component of the applied load, F_x^a, at a section defined by θ^2 is given by the following:

$$F_x^a = \int_0^{\bar{\alpha}} P \cdot \cos\alpha \cdot R \cdot d\alpha \qquad (4)$$

where p is given by Eq. (3) and α is defined by $\theta^1 = \alpha \cdot R$.

Rewriting Eq. (3) in terms of α and substituting into Eq. (4) one obtains

$$F_x^a = R \cdot P \int_0^{\bar{\alpha}} \cos\alpha \cos\frac{\pi}{2}\frac{\alpha}{\bar{\alpha}}\, d\alpha$$

The above integration yields

$$F_x^a = R \cdot P \cdot \frac{\frac{2\pi R}{\bar{\theta}^1}}{(\frac{\pi R}{\bar{\theta}^1})^2 - 4} \cdot \cos\frac{\bar{\theta}^1}{R} \qquad (5)$$

The component of the reactive load at a corresponding section is

$$F_x^r = \int_0^{\bar{\phi}} p_r \cdot \cos\phi \cdot R\, d\phi = p_r \cdot R \sin\bar{\phi} \qquad (6)$$

Equilibrium condition $F_x^r = F_x^p$ gives the reactive pressure:

$$p_r = \frac{P}{\sin\bar{\phi}} \frac{\frac{2\pi R}{\theta^{-1}}}{[(\frac{\pi R}{\bar{\theta}^1})^2 - 4]} \cos\frac{\bar{\theta}^1}{R}$$

$\bar{\phi}$ is the strap angle used in the actual experiments and assumed to be 60°.

In the MARC program the distributed loads are computed by numerical integration over each element. A subroutine defines the load magnitude point-by-point -- seven points are used per element in the element used in the present analysis. To check the accuracy of this procedure, independent integrations

of the total applied loads in the x-direction (Equation (5) integrated with respect to θ^2) and in the y-direction were performed. These values were checked against the total distributed load in the x and y directions which were internally calculated by the computer program for use in the stress analysis. The comparison of the values is as follows:

	ΣF_x^a	ΣF_y^a
Numerical Integration	229,311 lbs.	54,045 lbs.
Program	234,734 lbs.	54,391 lbs.
Deviation (percent)	2	0.6

RESULTS

A small displacement elastic analysis was performed. The numerical results were obtained in terms of displacement plots as well as contours of direct and equivalent stresses on the top and bottom surfaces of the shell.

Figure 2.5 shows the radial displacements on the symmetry plane along the length of the cylinder. In this analysis a maximum radial displacement of 3.39" occurred at the mid-section.

The cross-sectional deformation pattern is plotted in Figure 2.6 at the section where maximum radial displacement is obtained.

Figure 2.7 shows the y component of displacement on the y-z plane.

In the cylinder a maximum compressive hoop stress of 30,000 psi was obtained on the surface close to where the maximum pressure was applied. The stress was mainly caused by bending. At the same point the compressive axial

stress was 23,000 psi. It is noted, however, that a stress concentration occurs in the aft end sphere due to ovalization. A maximum compressive stress of about 51,000 psi was found in the hoop direction in the area (c) indicated in Figure 2.1.

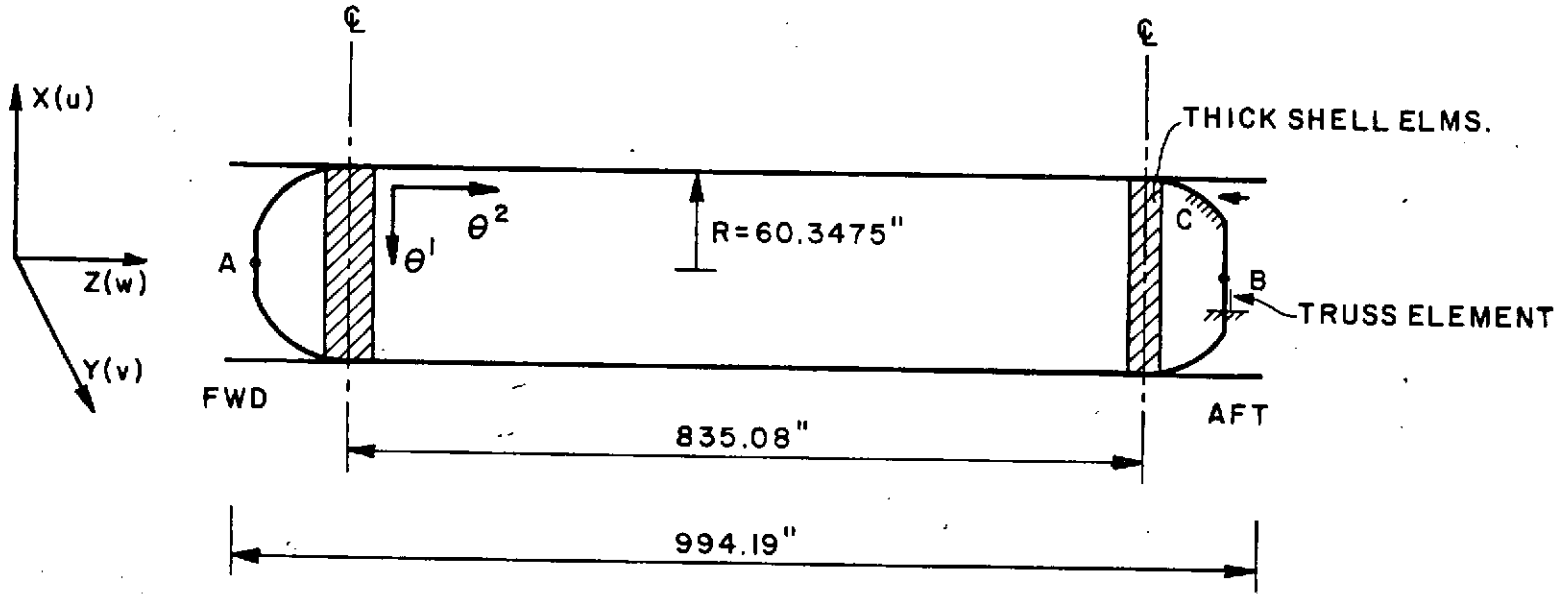

THICKNESS:
CYLINDER 0.347"
SPHERE 0.231"
THICK SHELL ELM. FWD: 0.444"
AFT: 0.534"

PROPERTY$_6$:
$E = 29 \times 10^6$ psi
$\nu = 0.32$

BOUNDARY CONDITIONS
SYMMETRY (XZ PLANE)

$$v=0, \frac{\delta v}{\delta \theta^2}=0, \frac{\delta u}{\delta \theta^1}=0, \frac{\delta w}{\delta \theta^1}=0$$

NODE A:

$$u=0, w=0, \frac{\delta w}{\delta \theta^1}=0$$

NODE B:

$u=0$

FIG. 2.1 STATIC TEST MODEL

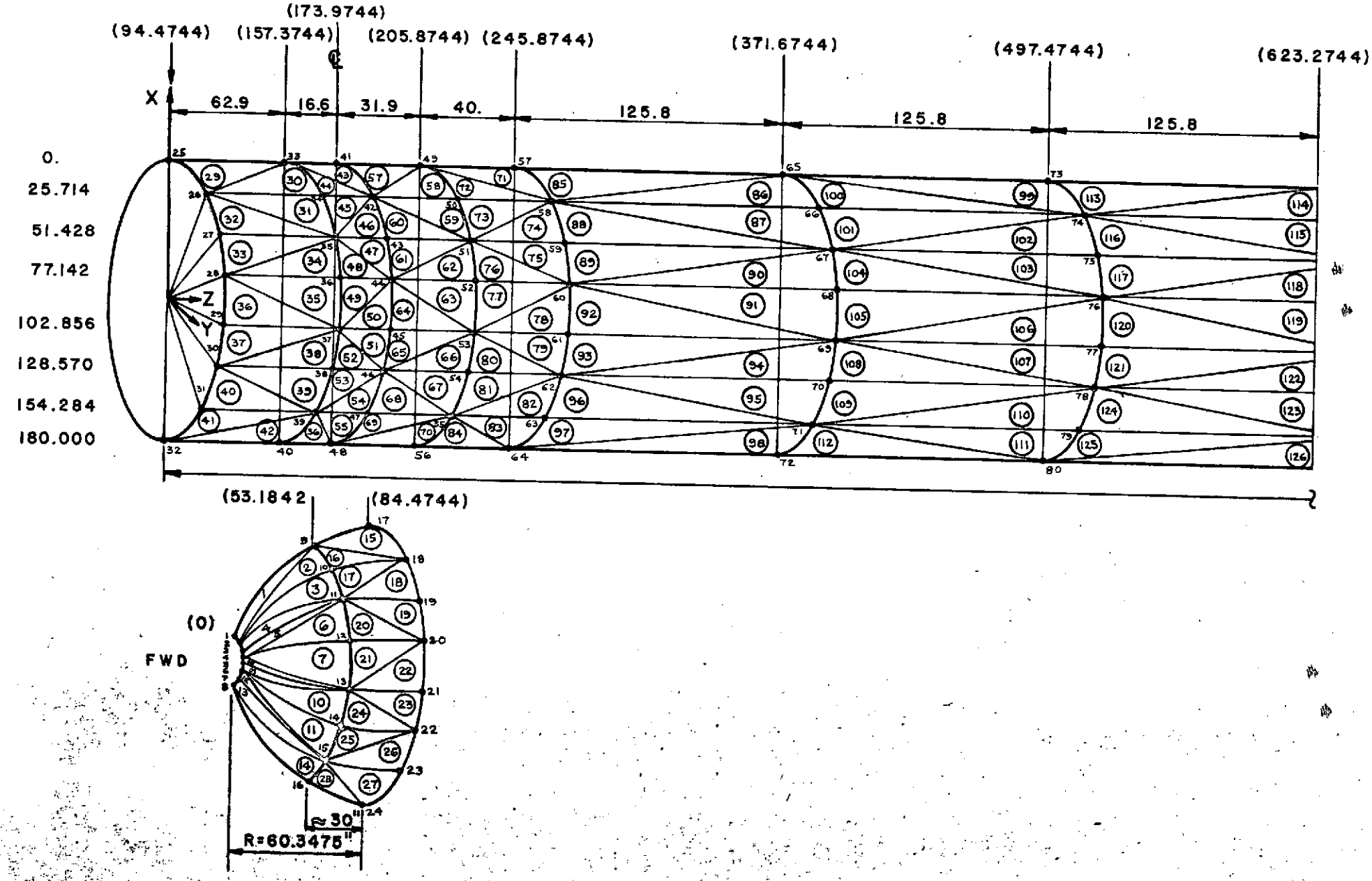

FIG. 2.2 FINITE ELEMENT IDEALIZATION

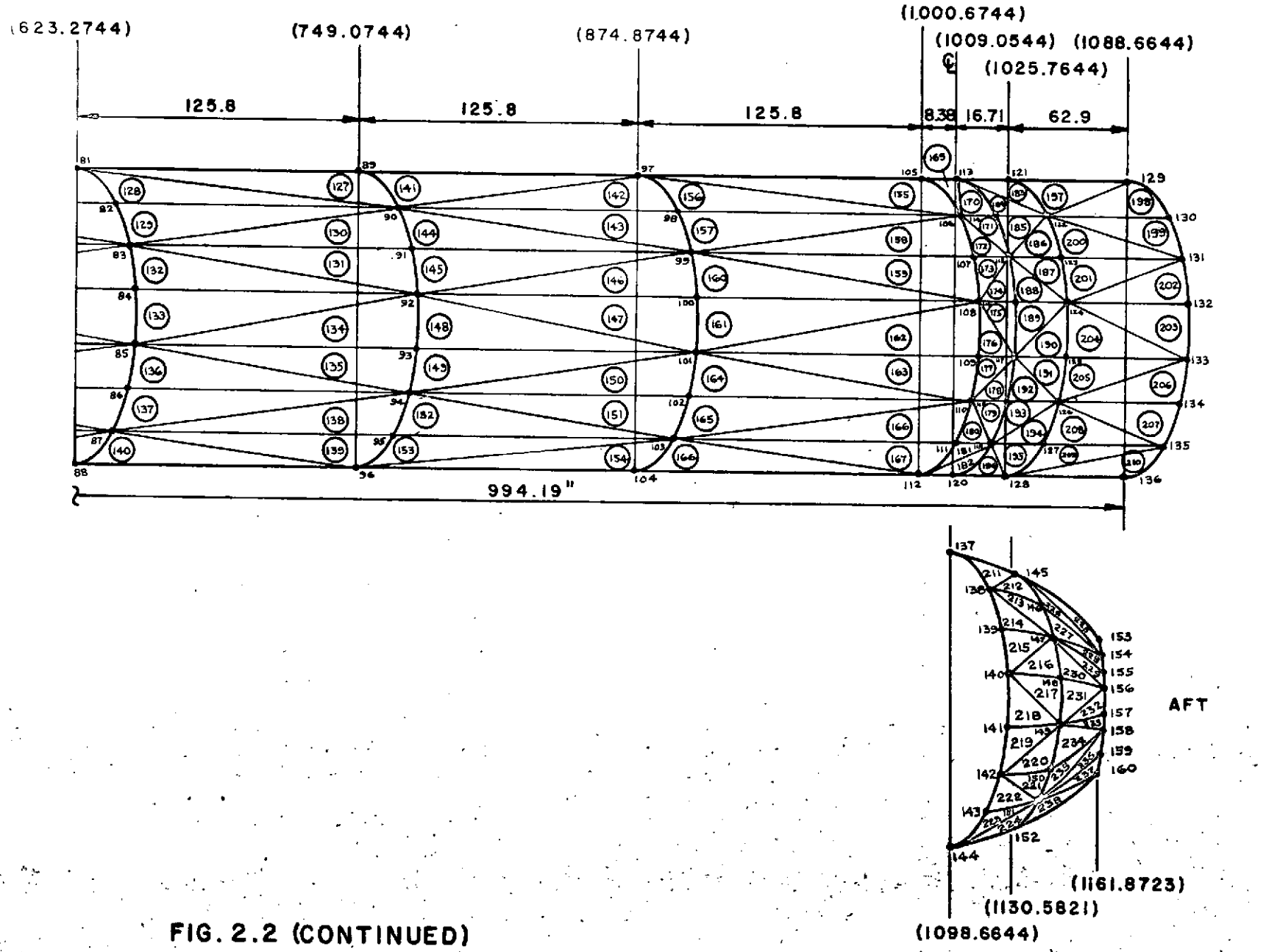

FIG. 2.2 (CONTINUED)

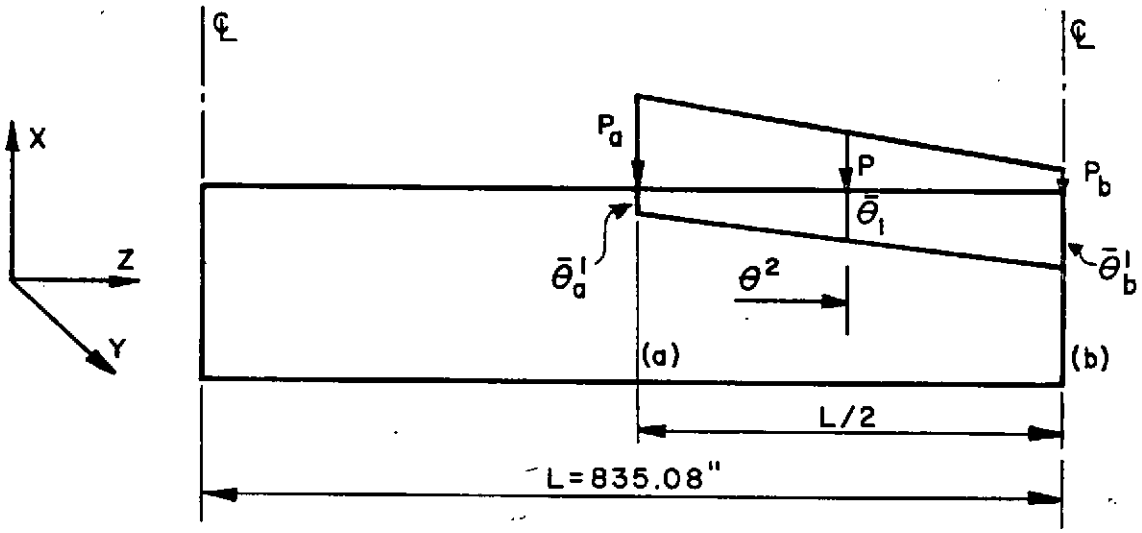

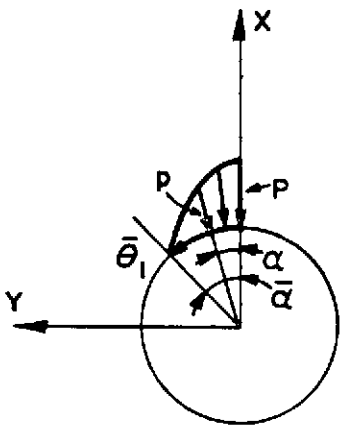

$\theta = \alpha \cdot R$

$\bar{\theta}' = \bar{\alpha} \cdot R$

$\bar{\alpha}_a = 15°$

$\bar{\alpha}_b = 60°$

FIG. 2.3 APPLIED PRESSURE

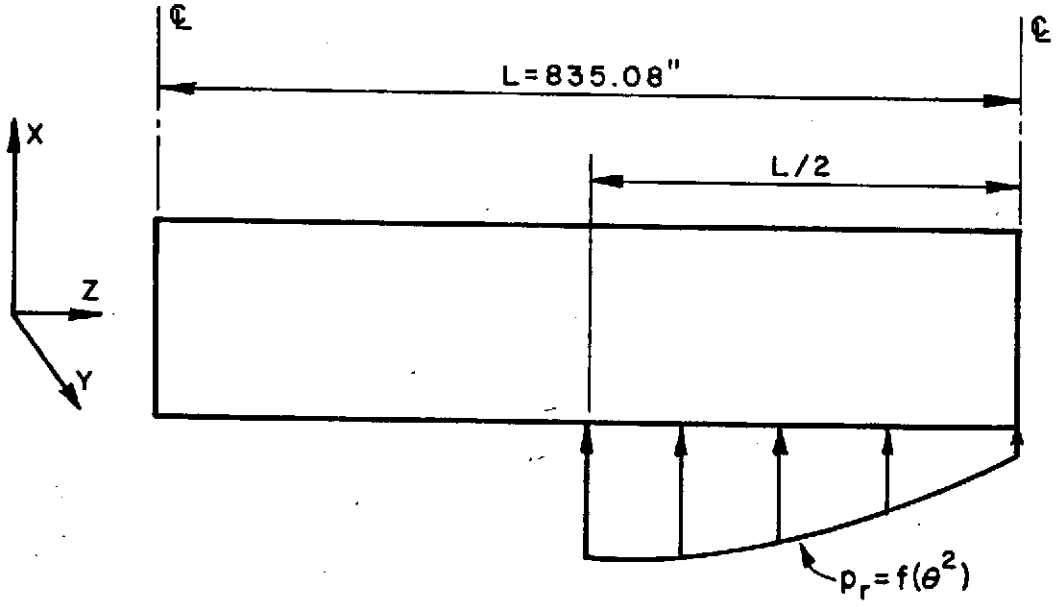

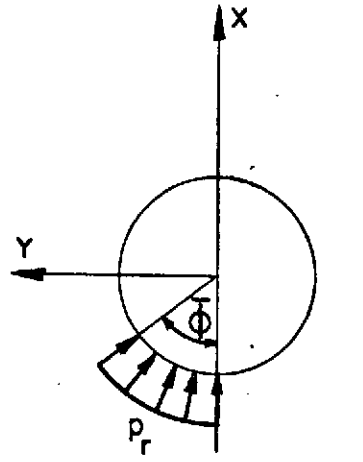

$\overline{\Phi}$ = 60° STRAP ANGLE

FIG.2.4 REACTIVE PRESSURE

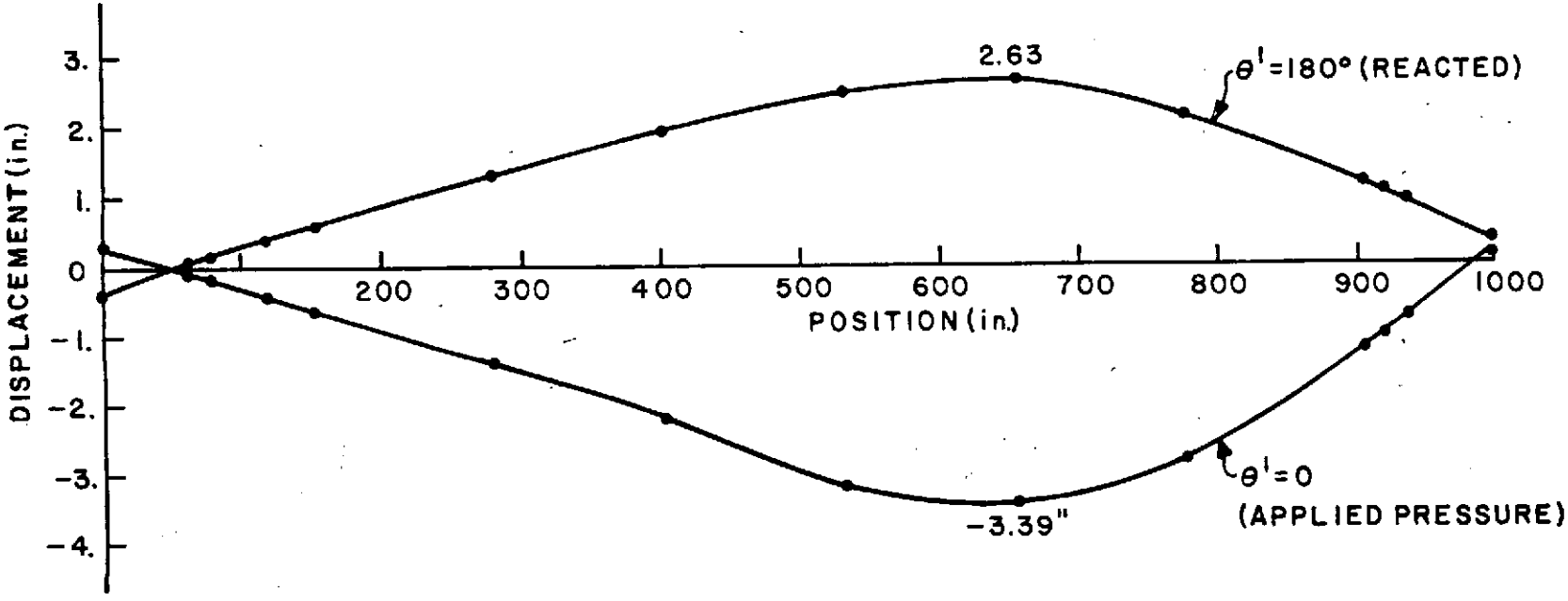

FIG. 2.5 RADIAL DISPLACEMENT PLOT ALONG THE CYLINDER

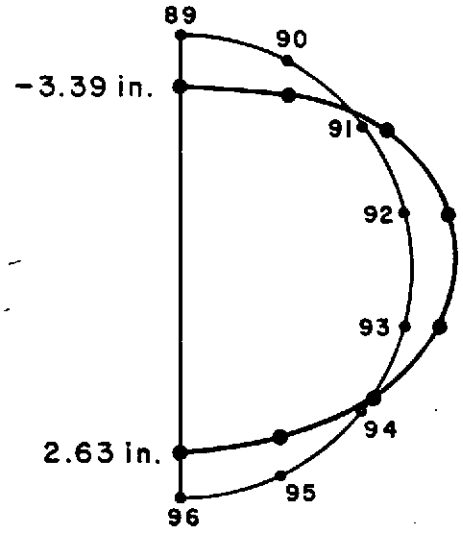

FIG. 2.6 CROSS-SECTIONAL DEFORMATION AT MID-SECTION

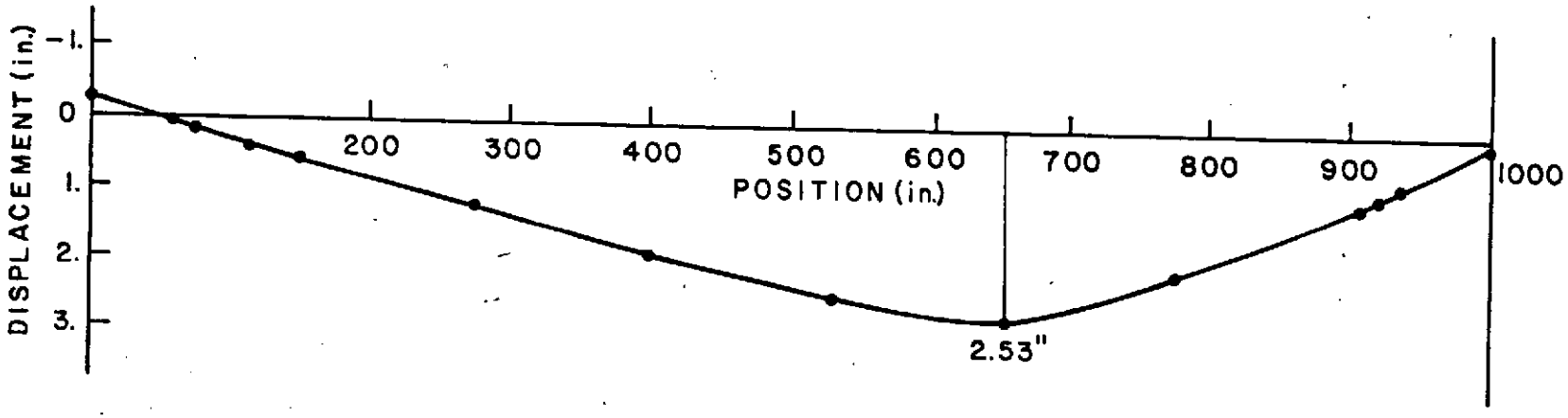

FIG.2.7 DISPLACEMENTS ON THE Y-Z PLANE

The geometric model was identical to that used for the strap load cases. This allows direct comparison between inertia and strap loads.

LOADING

The inertia loading is derived below. This derivation assumes that the casing behaves essentially as a rigid body during the deceleration, that is, that for the computation of d'Alembert forces the distortion may be neglected. Then referring to Figure 3.1, let the accelerations of the casing at (x, y, z) be a_x, a_y, a_z. From symmetry considerations and the rigid body assumption it follows immediately that

$$a_y = 0 \tag{1}$$

at all points.

The rigid body assumption gives additionally

$$a_x = A_x + z\,\ddot{\theta}_y$$

$$\text{and} \quad a_z = A_z - x\,\ddot{\theta}_y \tag{2}$$

where A_x, A_z are the translational accelerations of the point (0,0,0) in the x- and z-directions, and $\ddot{\theta}_y$ is the rotary acceleration of the same point about the y-axis.

The three equilibrium equations remaining after symmetry considerations (about the x-z plane) are

$$\int_S a_z \rho t \, dS = 0 \tag{3}$$

in the z-direction

$$\int_S a_x \rho t \, dS = \int_{S^1} p_x \, dS \tag{4}$$

in the x-direction

and $$\int_S (a_x z - a_z x) \rho t \, dS = \int_{S^1} z p_x \, dS \tag{5}$$

about the y-axis

where s is the surface of the casing,

S^1 is the surface subject to pressure,

p_x is the component of pressure in the x-direction

$t(\theta^1, \theta^2)$ is the shell thickness at a point (θ^1, θ^2)

and ρ is the shell density (assumed constant)

Equations (2) and (3) give immediately

$$A_z = 0 \tag{6}$$

since $t = t(z)$ is not a function of x.

Equations (2) and (4) give

$$\rho A_x \int_S t dA + \rho \ddot{\theta}_y \int_S zt \, dS = \int_{S^1} p_x \, dS \tag{7}$$

and (2) and (5) give

$$\rho A_x \int_S zt \, dS + \rho \ddot{\theta}_y \int (z^2 + x^2) \, tdS = \int_{S^1} z p_x \, dS \tag{8}$$

Equations (7) and (8) may be solved to give A_x and $\rho\ddot{\theta}_y$ as

$$\rho A_x = P_x \frac{\{I_y - z_c J_y\}}{\{V. I_y - J_y^2\}} \tag{9}$$

$$\rho\ddot{\theta}_y = \frac{P_x \{J_y - z_c V\}}{\{J_y^2 - V. I_y\}} \tag{10}$$

where $P_x = \int_{S^1} p_x \, dS$ = net external force in the x-direction

$z_c = \frac{1}{P_x} \int_{S^1} z \, p_x \, dS$ = center of influence of external pressure

$V = \int_S t dS$ = volume of shell

$J_y = \int_S zt \, dS$ = 1st moment of area of shell about the y-axis

and $I_y = \int_S (z^2+x^2) \, t dS$ = 2nd moment of area of shell about the y-axis.

The load case is then defined by

$p(\theta^1, \theta^2)$ on S^1 (as used in the previous analyses)

and d'Alembert forces $-\rho t a_x$ in the x-direction, $-\rho t a_z$ in the z-direction per unit surface area at all points of the shell.

The forces $-\rho t a_x$, $-\rho t a_z$ are available by combination of equations (9) and (10) with (2).

In practice the constants defined after equations (10) were computed numerically by suitable coding in the shell element in MARC, resulting in the following values:

$$P_x = -2.347 \times 10^5 \text{ lb}$$

$$z_c P_x = -1.6207 \times 10^8 \text{ lb-in}$$

$$V = 7.20881 \times 10^4 \text{ in}^3$$

$$J_y = 3.569 \times 10^7 \text{ in}^4$$

$$I_y = 2.44714 \times 10^{10} \text{ in}^5$$

Then the coding was further modified to include $-\rho t a_x$ and $-\rho t a_z$ as forces on the shell in the x- and z-directions. This technique (using numerical development of the inertia loads) made the inertia load analysis quite straightforward. The values of P_x, z_c, and V were checked by approximate hand-calculation to eliminate gross programming errors.

RESULTS

The results of this analysis are summarized in Figures 2-9. Figure 3.2 shows the cross-sectional distortion at the most severely distorted section of the main cylinder. Figure 3.3 shows radial displacements on the x-z plane (the symmetry plane). In both cases the strap loaded case (static test case) results are shown for comparison. It may be seen that the inertia case always gives significantly less deformation. Comparison with the static model results shows rather similar stress distributions, but with reduced magnitude in the inertia load case. The equivalent stresses in the last ring of elements of the aft closure (the most highly stressed elements) are compared in Table 3.1 with the linear analysis results for the strap loaded case.

DISCUSSION

In general the comparison with the strap loaded case indicates that, while the static test rig should predict the deformation mode with reasonable accuracy, the magnitudes of the displacements in such a test are 30% too high for the actual inertia loads and peak stresses are 60% too high. This is intuitively explained by noting that the net reaction from the strap includes a significant y-direction component not present in the inertia load. This should tend to increase the stress levels, but reduce the distortion. More significantly, the inertia load is generated uniformly around the circumference, while the strap load is confined to the lower of 120° segment. Thus, some of the pressure load is reacted directly by inertia loads, while in the strap loaded case all of the pressure load must be carried around to the opposite side of the shell. It is this difference which seems most likely to give the large differences in stress and displacement magnitudes. The fact that the deformation modes are so similar suggests that the geometry renders the structure relatively insensitive to the distribution of particular load components, since in one case (straps) the load is confined to one section of the casing, while in the other case (inertia), while the net loads must be the same, the distribution is rather more uniform.

	EQUIVALENT STRESS (psi)			
	INSIDE		OUTSIDE	
Element Number	Strap Reacted	Inertia Reacted	Strap Reacted	Inertia Reacted
225	21592	13543	50711	31525
226	18004	12131	16886	10757
227	17552	11261	27211	17407
228	39549	24317	12128	7830
229	31012	18718	21071	13722
230	15867	9520	22520	13227
231	15635	9447	15182	9812
232	11227	6977	46572	27973
233	32745	20112	41425	24621
234	16288	9411	20792	12106
235	17056	10085	24579	14569
236	39022	23514	27150	16558
237	18928	11573	36178	22135
238	14995	8772	18574	11381

TABLE 3.1 EQUIVLANET STRESS IN END RING OF ELEMENTS ON AFT CLOSURE

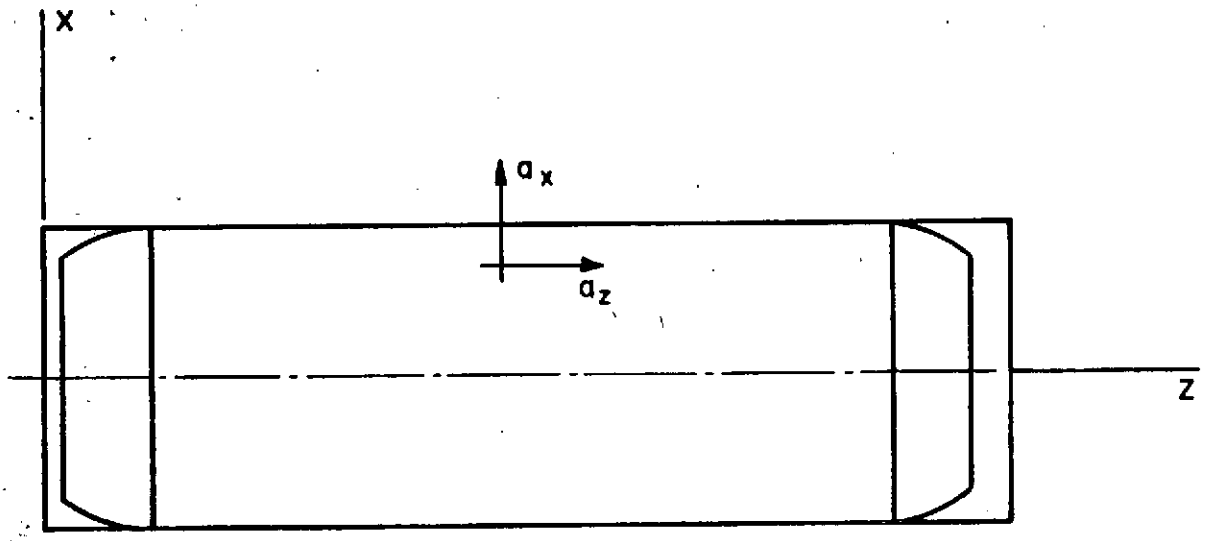

FIG.3.1 ACCELERATION COMPONENTS

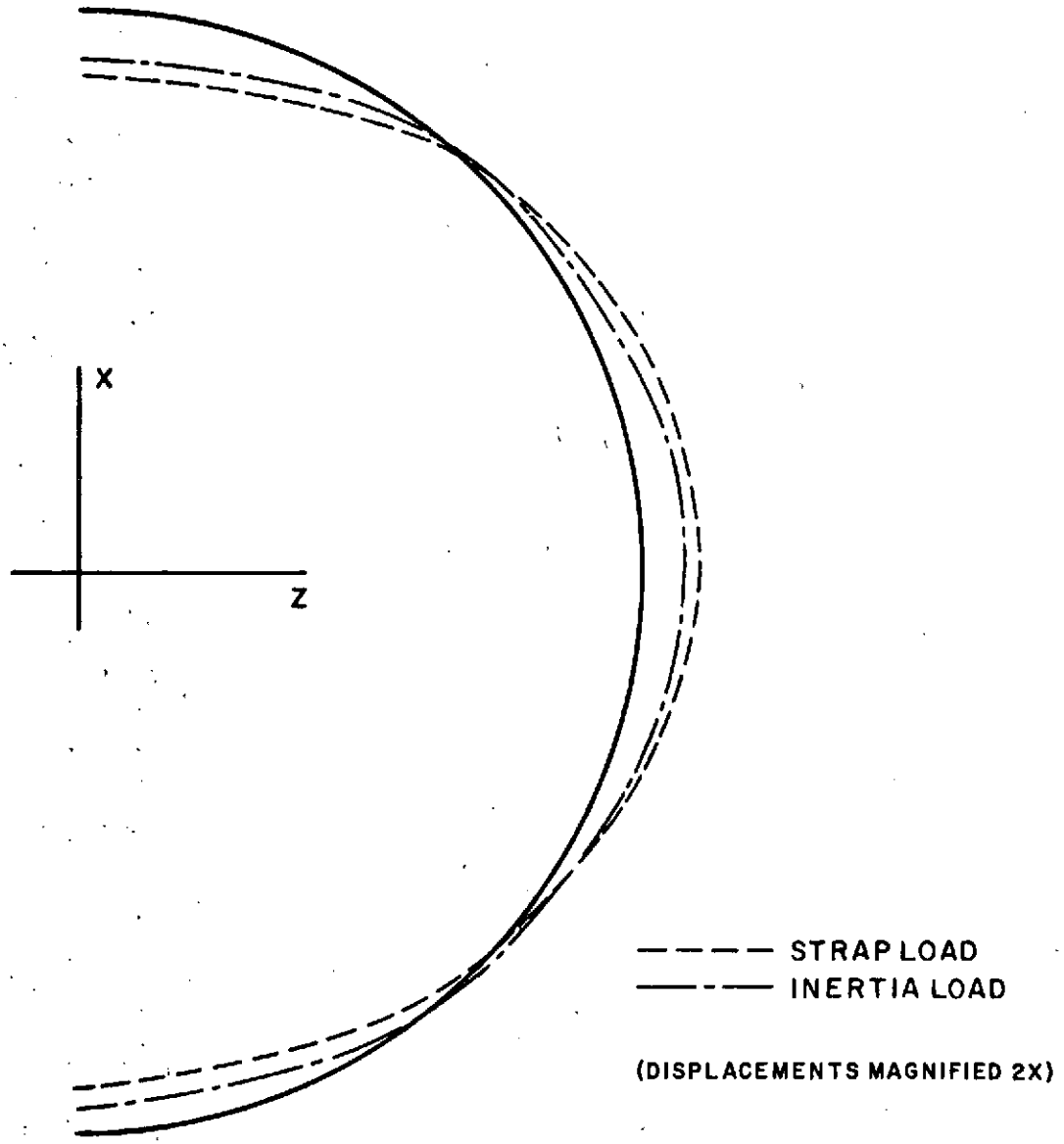

FIG. 3.2 DISTORTION OF SECTION, NODES 89-96 (Z = 655")

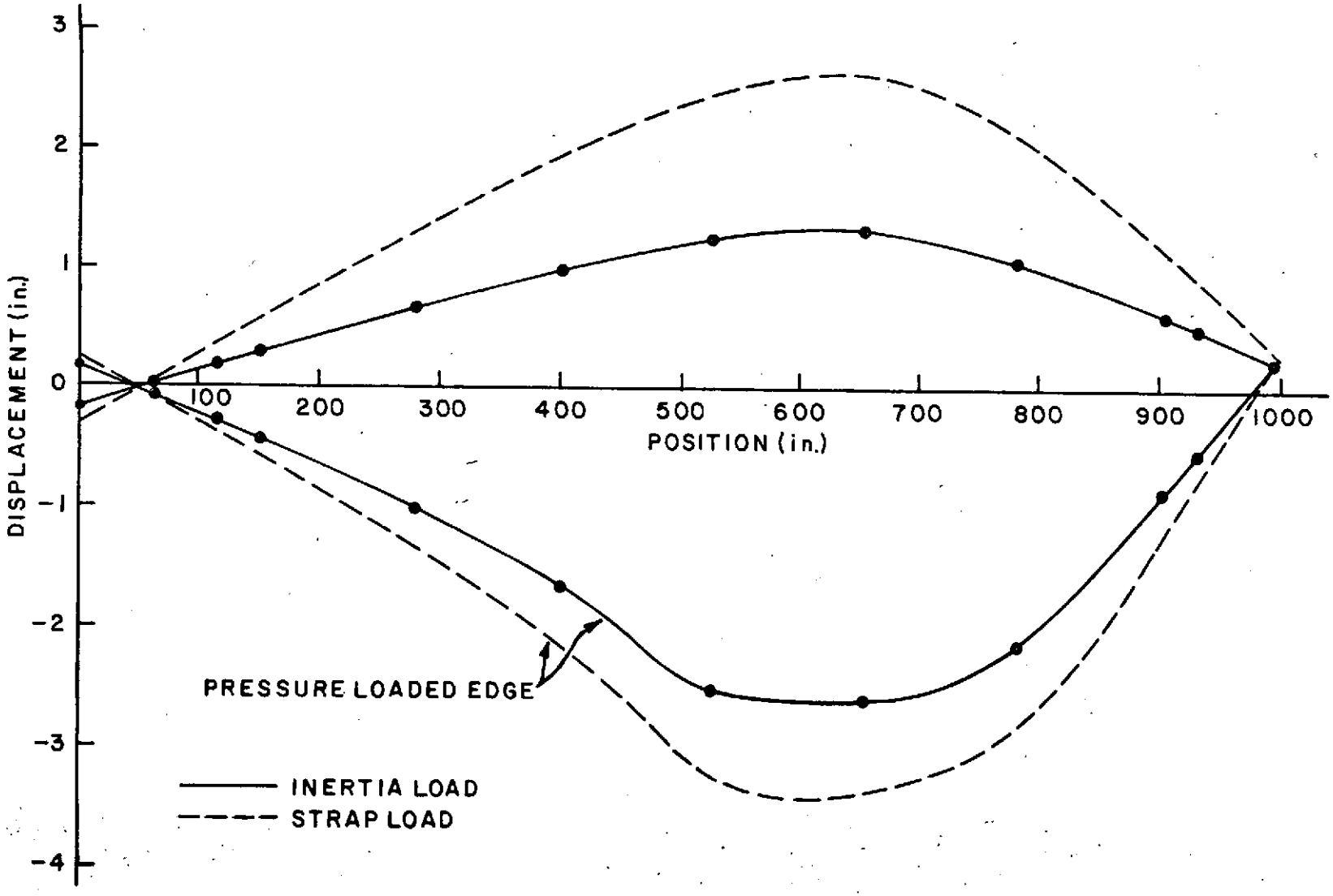

FIG. 3.3 RADIAL DISPLACEMENT ON SYMMETRY PLANE

At this point in time the first results from the tests of the static model and parallel analysis at NASA with NASTRAN and BOSOR suggested that the results from MARC were four times too stiff. The NASTRAN analysis with 2000 elements in an octant model predicted a mid-section displacement of 12.8 ins. in the static test and BOSOR predicted 13 ins. A mesh convergence study was then performed with a simplified model with the same governing parameters as the solid rocket motor booster to try to explain this discrepancy.

In order to study the element efficiency for the actual rocket motor problem, a smaller, simpler analysis problem was investigated. This problem was felt to have the essential characteristics of the actual problem, but is of considerably smaller size, so that mesh convergence experiments were not prohibitively expensive. This section describes this smaller problem, and the results obtained.

MODEL

The model is one-eighth of a circular cylinder, with symmetry conditions on three edges and diaphragm support on the third (Figure 4.1). The loading is a normal pressure with the same distribution as that of the real problem (Figure 4.2).

The pressure p at a general point (θ^1, θ^2) is given by the following expression:

$$p\,(\theta^1, \theta^2) = \left[\frac{P_b - P_a}{\theta_b^2 - \theta_a^2}\,(\theta^2 - \theta_a^2) + P_a\right] \cdot \cos\left[\frac{\pi}{2}\left(\frac{\theta^1}{\frac{\theta_b^1 - \theta_a^1}{\theta_b^2 - \theta_a^2}\,(\theta^2 - \theta_a^2) + \theta_a^1}\right)\right]$$

The numerical values assumed for the present analysis are:

$$\left.\begin{aligned} P_a &= 45.\ \text{psi} \\ P_b &= 8.\ \text{psi} \end{aligned}\right\} \text{ peak values of pressure on symmetry plane}$$

$$\left.\begin{aligned} \bar{\alpha}_a^1 &= 15^\circ \ (\bar{\theta}_a^1 = \bar{\theta}_a^1 \cdot R) \\ \bar{\alpha}_b^1 &= 60^\circ \ (\bar{\theta}_b^1 = \bar{\theta}_b^1 \cdot R) \end{aligned}\right\} \text{circumferential extents of pressure loading}$$

Where θ^1 and θ^2 are the Gaussian surface coordinates with $\theta^1 = R\alpha$, $\theta^2 = z$.

Small displacement, linear elastic behavior was assumed.

ELEMENTS

Two thin-shell elements were used in this convergence test. Both use Koiter-Saunders shell theory, and both have C^1 continuity (piecewise C^2). Rigid body motions are represented exactly because of the isoparametric formulation of the elements. Loading was generated by consistant distribution. The triangular element is the Dupuis Element [1] which uses cubic interpolation corrected by rational functions. The quadrilateral element is a simple bicubic element using the nodal degrees of freedom

$$u^i, \frac{\partial u^i}{\partial \theta^1}, \frac{\partial u^i}{\partial \theta^2}, \frac{\partial^2 u^i}{\partial \theta^1 \partial \theta^2}, \quad i=1,2,3$$

at four nodes. This element is described by VerHague and Mallett in [2]. It should be noted that the element is only admissible as a rectangle in the (θ^1, θ^2) plane (the mapped plane of surface coordinates). This is not as severe

a restriction as might first be thought, since any surface coordinate set (θ^1, θ^2) is allowable. However, the element is probably only useful for problems of the present type, where a regular mesh is satisfactory both in the θ^1-θ^2 plane and on the real surface. For such problems, the element is ideal, since it is easy to form because of its straightforward interpolation functions, and is cheap to run, since nine (Gaussian) integration points in the $(\theta^1$-$\theta^2)$ plane prove sufficient.

RESULTS

In all cases regular grid spacings were used. The Dupuis element was used with five meshes: 4x6 divisions, 4x8, 6x8, 6x10 and 8x10, where the divisions around the quarter circumference are given first. The bicubic element was used with three meshes; 2x2, 3x3 and 4x4 elements. Further meshes were not run because it was felt little additional improvement would be obtained. The displacement results are characterized by the peak x-direction displacement (at the top center of the cylinder) in Figure 4.3. These indicate that any of the bicubic meshes gives an essentially converged solution, while the Dupuis triangle shows rather slow convergence. This came as a surprise, since the Dupuis element has shown rapid convergence in the classical cylindrical roof problem of Scordelis and Lo [3]. However, the relatively poor performance of the triangle was observed in some problems by Dupuis [3].

CONCLUSIONS

The above mesh convergence study was taken to indicate that the Dupuis element was unsuitable for the rocket motor casing analysis, but that the bicubic element would provide reliable results with any reasonable mesh spacing. The convergence studies included small displacement, linear elastic behavior only, but because of the completeness of the element formulation (and its isoparametric form), it was anticipated that it should give comparably good results

in the nonlinear range. Indeed, an axisymmetric form of this element was shown to have excellent convergence properties by McNamara [5].

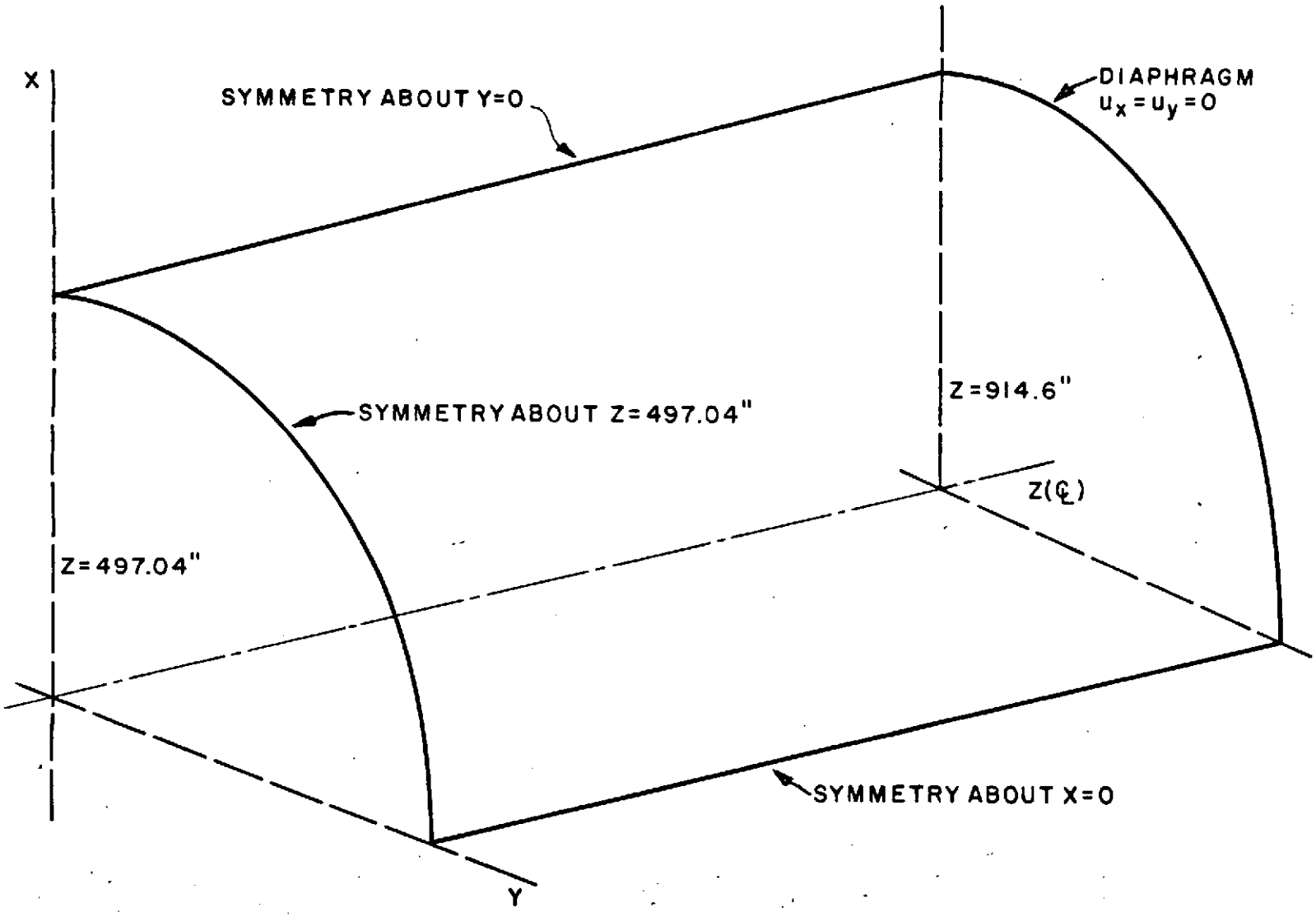

R = 60.35", t = 0.347"

$E = 29 \times 10^6$ psi, $\nu = 0.32$

FIG. 4.1 MODEL GEOMETRY

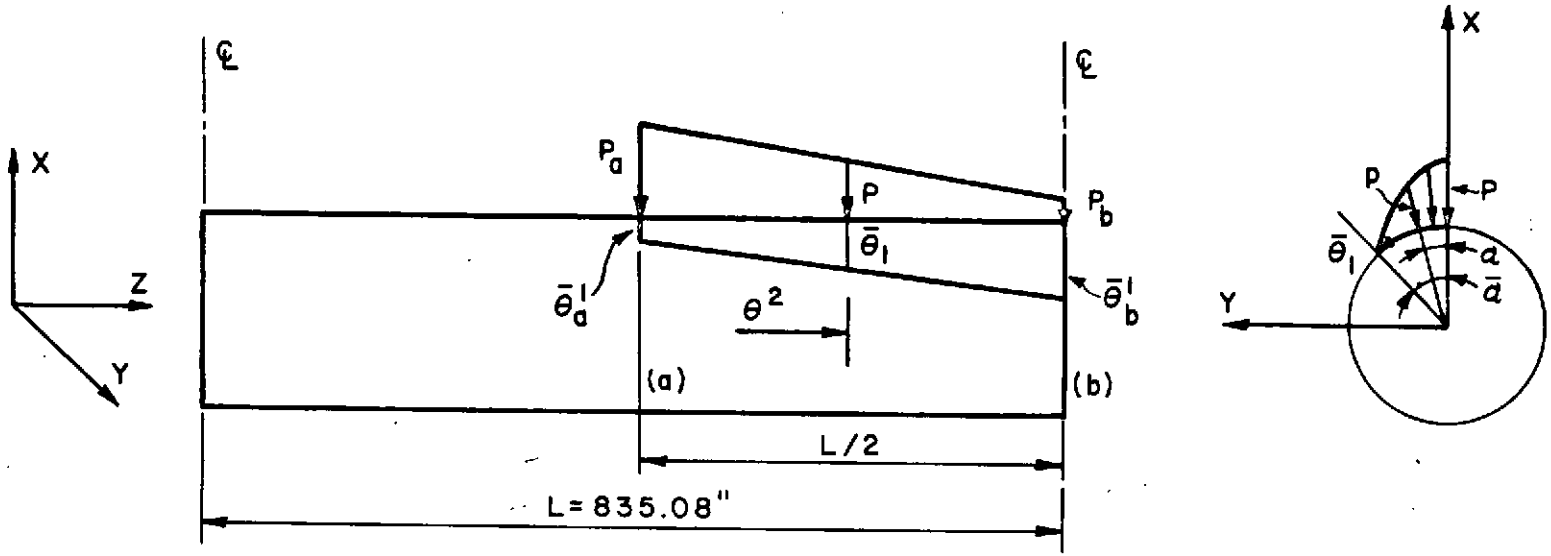

$\theta = \alpha \cdot R$

$\bar{\theta}' = \bar{\alpha} \cdot R$

$\bar{\alpha}_a = 15°$

$\bar{\alpha}_b = 60°$

FIG. 4.2 APPLIED PRESSURE

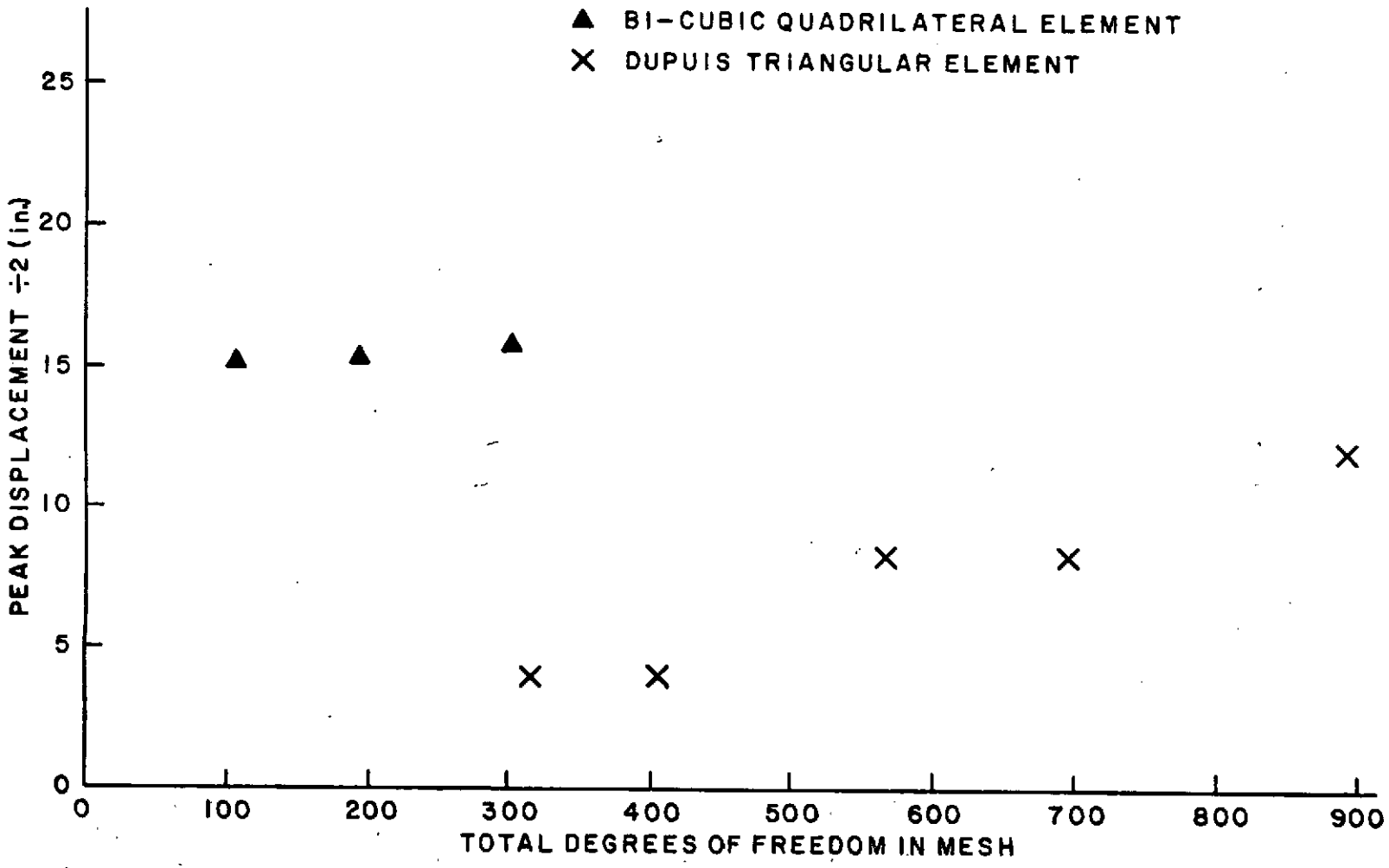
▲ BI-CUBIC QUADRILATERAL ELEMENT
× DUPUIS TRIANGULAR ELEMENT
PEAK DISPLACEMENT ÷2 (in.)
25
20
15
10
5
0
0
100
200
300
400
500
600
700
800
900
TOTAL DEGREES OF FREEDOM IN MESH

FIG. 4.3

With the results of the mesh convergence study in hand, it was decided to reanalyze the static and inertia loading cases.

This section covers a linear comparison between static (strap-reacted) and inertia loadings of the 120" rocket motor casing. This analysis is preliminary to a similar comparison, based on non-linear incremental analysis. In all cases the pressure pad is on the aft half cylinder, with its peak at the mid-section of the cylinder. This linear comparison has been made before in section 3. The difference is that the present analysis uses a higher order quadrilateral shell element which has been shown to give rapidly convergent displacement solutions for this type of loading in section 4.

MODEL

The modelling is of the same 120" casing described in previous sections. The use of the new quadrilateral shell element allowed modelling with a coarser mesh at small penalty in solution accuracy, with considerable savings in computer cost. The geometric model assumed for the present analysis is shown in Figure 5.1a, and the mesh used is shown in Figure 5.1b.

Several points must be emphasized with regard to this geometric modelling:

1. Uniform thickness has been assumed throughout the cylinder. This is an unrealistic, but conservative assumption. The difficulty with the inclusion of thickening effects is that the thickened lengths are quite short compared to the element size used in the analysis. Because of the cost of mesh refinement to capture thickening effects it was decided to use

the un-thickened model. Thickening could be achieved through the use of beam elements as stiffeners at the joints. While this approach is adequate for small displacement elastic analysis, stress predictions are not very good, so that this modelling is unsuitable for non-linear work. It must be emphasized that the un-thickened model will give conservative results, because the peak stresses occur at the aft (loaded) cylinder/sphere joint, which should be thickened.

2. The aft spherical closure has been modelled as a complete hemisphere. Previous analyses by MARC have assumed a 60" opening in this closure, with no additional stiffness. Our analysis with the new quadrilateral shell element showed this end condition to be a most critical parameter, for both the peak displacements on the cylinder and the stressing of the closure itself. A strap-reacted analysis with the open ended, unstiffened closure showed severe ovalization of the sphere with associated high stresses. The closed end model was adopted after discussion with NASA personnel, since the actual casing would have some additional stiffness at this point from the nozzle and other members. The complete closure assumed here may possibly be over-stiff, in which case stresses on the closure would be under-estimated.

3. The mesh convergence tests indicated that a course mesh would be adequate for displacement predictions with the new shell element. Since the non-linear analysis

will be quite lengthy, it was decided to remesh with 5 sections around the half model (180°) and 12 sections along the cylinder. The results reported in section 4 indicate that this mesh spacing will give reliable displacement predictions for pressure pad loading. The linear analyses reported here took about 12 minutes each on a CDC 6600 - a considerable savings over previous analyses.

LOADING

The loadings used in the present analysis follow the same patterns reported previously. In both cases the pressure distribution is the same as that shown previously in Figure 2.4. Since the load is distributed by numerical integration in the program, check sums are compared to an 'exact' integration. These sums give the net force in the x (vertical) and y (horizontal) direction due to the pressure on the half cylinder: their values are as follows:

	F_x (lb)	F(lb)
'Exact'	229311	54045
Previous Triangular element mesh	234734	54391
Present Quadrilateral element mesh	228500	53793

For the inertia case, rigid body acceleration fields, a_x (x, y, z) were computed by the technique defined in section 3. The five constants defining the acceleration fields are again computed numerically; the following table compares their values:

	Previous Triangular Element Mesh	Current Quadrilateral Element Mesh
Total Vertical Load, P_x	-2.347×10^5 lb	-2.285×10^5 lb.
Moment of x Component of pressure about O_y, $z_c \cdot P_x$	-1.6207×10^8 lb-in	-1.5898×10^8 lb-in
Volume of Casing, V	7.2088×10^4 in^3	7.0629×10^4 in^3
First Moment of Casing about O_y, J_y	3.569×10^7 in^4	3.5128×10^7 in^4
Second Moment of Casing about O_y, I_y	2.4471×10^{10} in^5	2.4033×10^{10} in^4

RESULTS

a) Displacements

Displacement modes are quite similar in the two loading cases, with rather different peak displacement magnitudes. The displaced profiles of the top (pressure loaded) and bottom edge are shown in Figure 5.2 (scaled to 45 psi peak pressure), and the distorted shape of the most severely deformed radial section is given in Figure 5.3. Note the asymmetry about the plane x = 0: both the shape and magnitude of the vertical displacements (Figure 5.3) are quite different for the two edges. This would suggest that analyses based on the assumption of symmetry about

the plane x = 0 would overpredict the displacement and stress response under pressure loading since the reactive loading (inertia or strap) produces a less distortion on the opposite side of the shell. That is, symmetry about x = 0 would be an overly conservative assumption.

Peak displacement magnitudes, scaled to 45 psi peak pressure, are as follows:

	Strap Reacted	Inertia Reacted
Displacement at node 61	17.3"	13.6"

An explanation of the reduction in displacement response was offered in [1]. This displacement is basically the same as the NASTRAN and BOSOR predictions. It should be noted that this analysis is for a half model as opposed to the quarter models used for the NASTRAN and BOSOR analysis.

b) Stress

Peak stresses now occur at the intersection of the cylinder with the aft spherical closure. This is in contrast to the previous comparison. [1], where peak stresses occurred on the spherical closure, because of the ovalization allowed by the unstiffened hole in the aft sphere of that analysis. Peak stresses, scaled to 45 psi peak pressure, predicted by the present analysis are as follows:

	Strap Reacted	Inertia Reacted
Equivalent Stress (psi)	87440	68420
Hoop Stress (psi)	59530	46860
Axial Stress (psi)	53400	34550

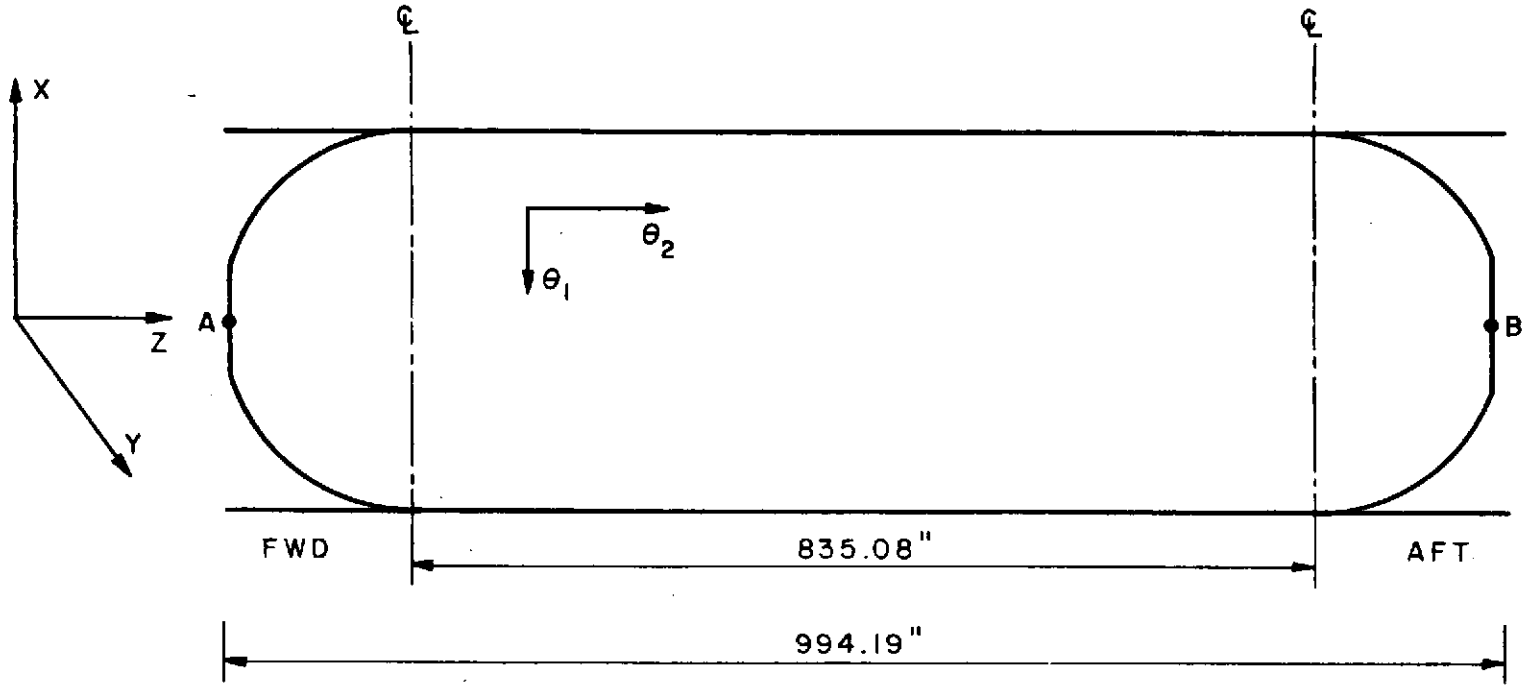

THICKNESS:
CYLINDER 0.347"
SPHERE 0.231"

PROPERTY:
$E = 29 \times 10^6$ psi
$\nu = 0.32$

BOUNDARY CONDITIONS SYMMETRY (XZ PLANE)

$$v = 0, \frac{\delta v}{\delta \theta^2} = \frac{\delta u}{\delta \theta^1} = \frac{\delta w}{\delta \theta^1} = \frac{\delta^2 u}{\delta \theta^1 \delta \theta^2} = \frac{\delta^2 w}{\delta \theta^1 \delta \theta^2} = 0$$

NODE A: $u = w = 0$ NODE B: $u = 0$

FIG. 5.1a TEST MODEL

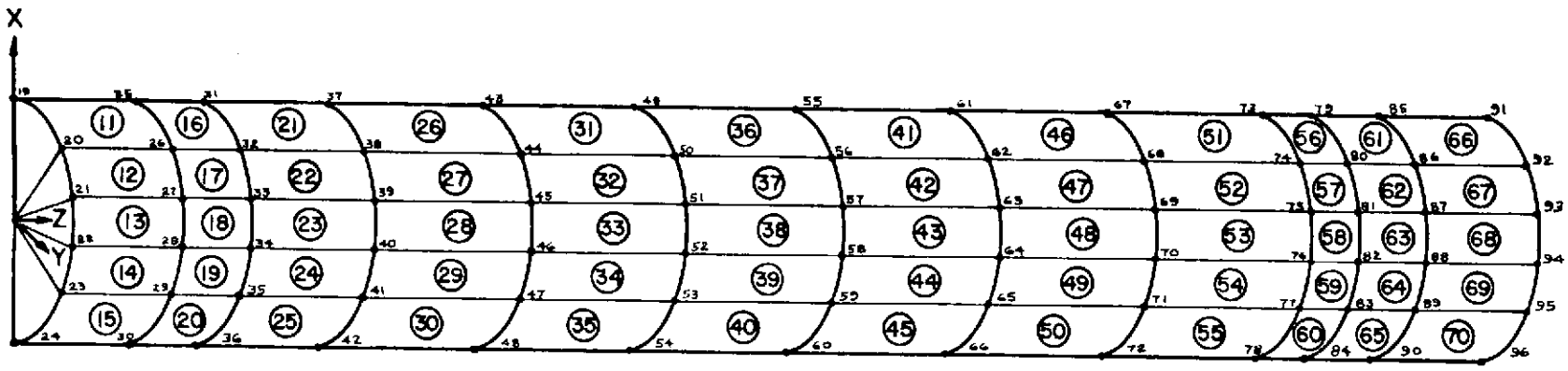

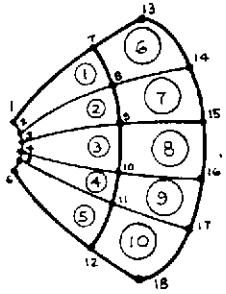

FWD

NUMEL = 80
NUMNP = 109

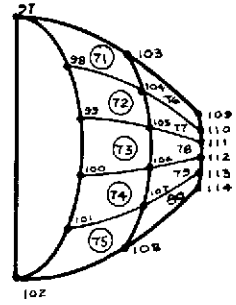

AFT

FIG. 51b TEST MESH

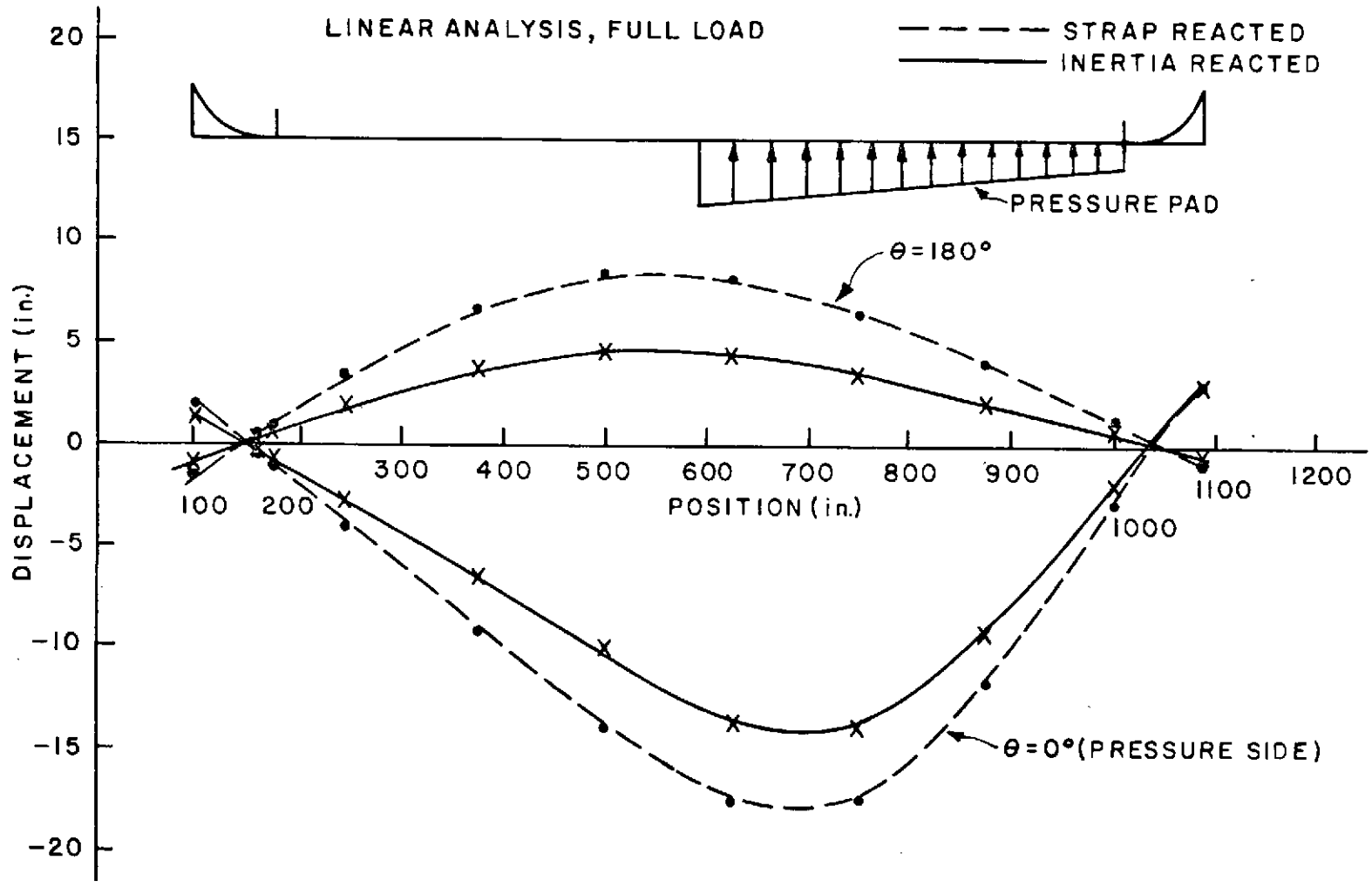

FIG. 5.2 RADIAL DISPLACEMENTS

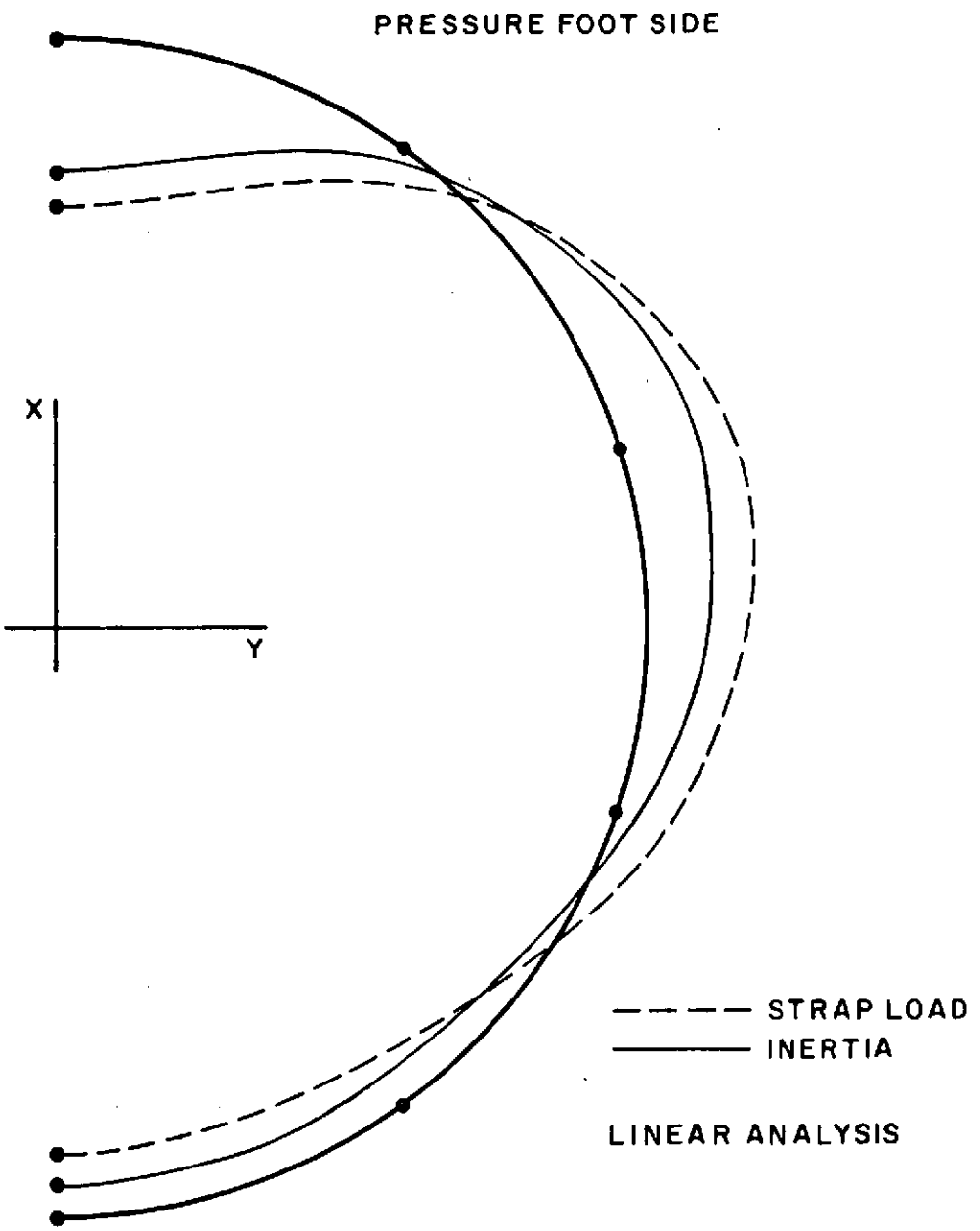

FIG. 5.3 CROSS SECTIONAL DISTORTION NODES 61-66 (Z=654.6")

NONLINEAR ANALYSIS FOR INERTIA LOAD WITH AND WITHOUT INTERNAL PRESSURE 6

This section describes the results of two non-linear incremental analyses of the 120" rocket motor casing. The difference between the two analyses lies in the loading and geometry of the model. The loading pattern in the first analysis is the same as analyzed previously (section 3), but applied incrementally using initially steps of 10% of full load (40 psi peak pressure). The second analysis uses an additional uniform internal pressure of 2 psi together with incremental loading of the external load pattern, in 5% steps.

MODEL

The geometric model assumed for the non-linear analysis with no internal pressure was identical to that analyzed previously described in section 3. For the analysis including internal pressure the model was modified so that the forward spherical cap was closed. The quadrilateral shell element described in section 4 was used in both models with the same mesh used in section 5. The model is shown in Figures 5.1 and 5.1a.

It must be emphasized that the geometry used assumes constant thickness throughout the cylinder. The actual motor casing has thickened joints, so that the model is assumed to yield conservative results.

LOADING

The loading patterns used in these non-linear analyses were identical to those used previously, with an inclusion of 2 psi internal pressure in the second analysis. Since the models are almost identical (the only difference is the inclusion of a closed forward sphere in the internal pressure case) the rigid body acceleration fields, a_x (x,y,z), remained essentially unchanged and the values reported in section 3 were used for both analyses.

RESULTS

a) Displacements

The displacements obtained from the two non-linear analyses are quite similar in mode because the external loading dominates the internal pressure. Figure 6.1 plots the distorted shape of the most severely deformed nodal section at maximum load reached. As was evident in the analysis of section 3 there is no symmetry about the plane x=0.

Figure 6.2 and Figure 6.3 show the displaced profiles of the top (pressure loaded) and bottom edges at maximum load reached in the two load cases. Again the asymmetry is evident. Note, however, that although the radial displacements are very similar in both mode and magnitude, the results of the analysis run with 2 psi internal pressure correspond to 45% of full load, whereas the results of the analysis with no internal pressure are at 35% of full load. The solution does not converge to a specified tolerance after this load, indicating imminent collapse (stiffness singularity). Thus, the internal pressure is seen to stiffen the structure. This can be seen clearly on Figure 6.4 which presents load-displacement curves for node 61 (the most critical node).

b) Stress

Peak stress magnitudes calculated by the MARC program occur in Element 41 and are as follows:

	Internal p=0 psi (35% of full load)	Internal p=2 psi (45% of full load)
Equivalent Stress (psi)	32,200	50,000
Hoop Stress (psi)	27,217	52,300
Axial Stress (psi)	26,500	36,611

Stress components and the equivalent stress are contoured for both analyses in Figures 6.5 - 16. These stresses are shown for the highest loads applied in each case. There is a high degree of similarity in the stress patterns in the two cases with the highest stresses occurring under the loading pad.

Figure 6.17 plots stresses versus % load for the centroid of the highest stressed element, Element 41. Notice that for the 10% load incrementation case (no internal pressure) the solution in stress oscillates significantly between increments. For the 5% load incrementation analysis (2 psi internal pressure), the solution is much more stable until after 30% application of peak load. This is the usual behavior as the collapse load is reached.

Recall that the internally pressurized case withstood 45% of full load as opposed to 35% in the non-pressurized analysis. This extra 10% of load explains the sizeable differences in the peak stresses noted above.

It must also be remembered that the results presented here are conservative since there is no account taken of the thickening of the joints due to the spherical-cylinder intersection.

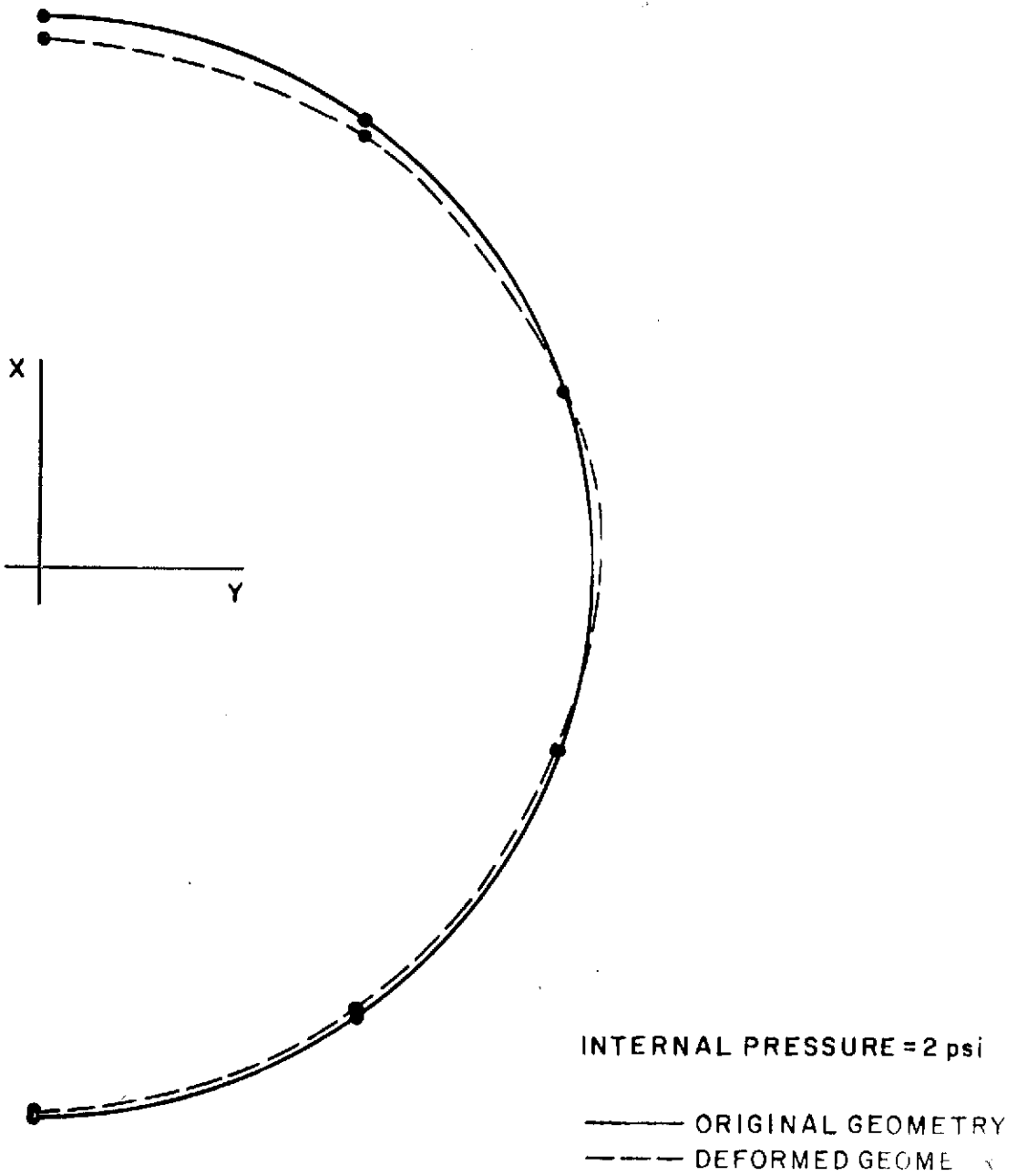

FIG. 6.1 DEFORMATION OF CROSS SECTION AT PEAK PRESSURE

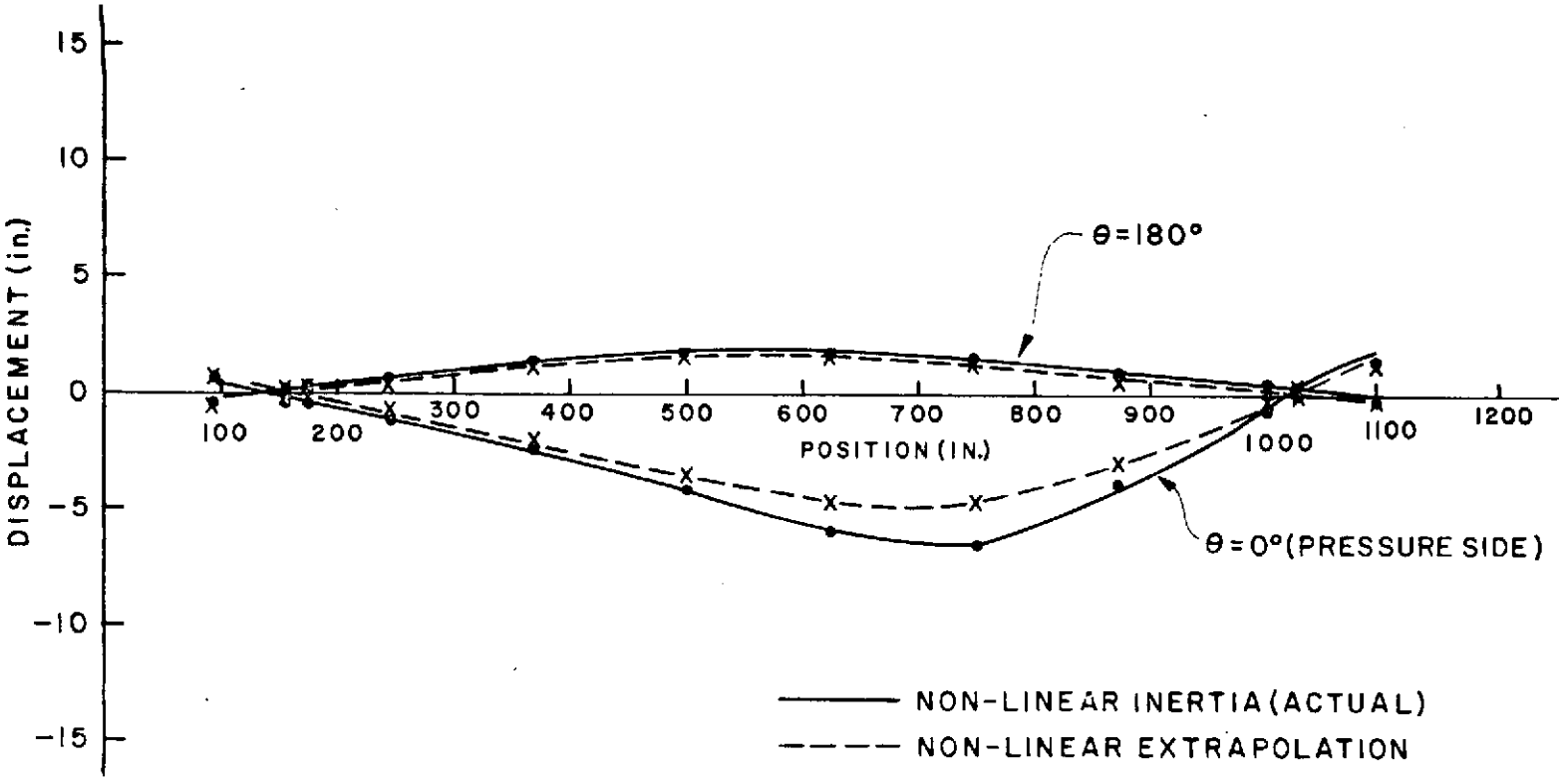

FIG. 6.2 RADIAL DISPLACEMENT (35 % LOAD) INTERNAL p=0

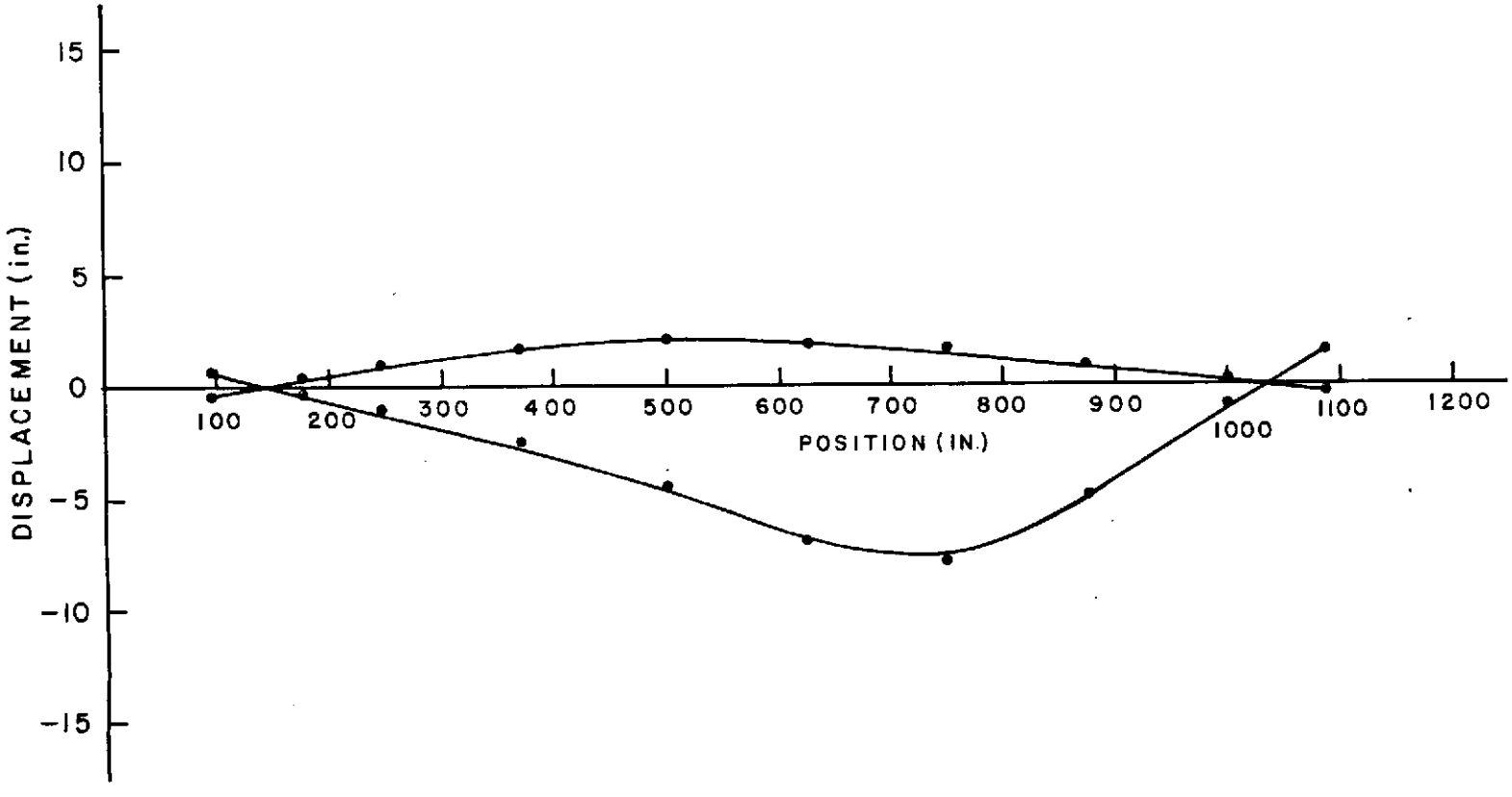

FIG. 6.3 RADIAL DISPLACEMENT (45% LOAD) INTERNAL p=2

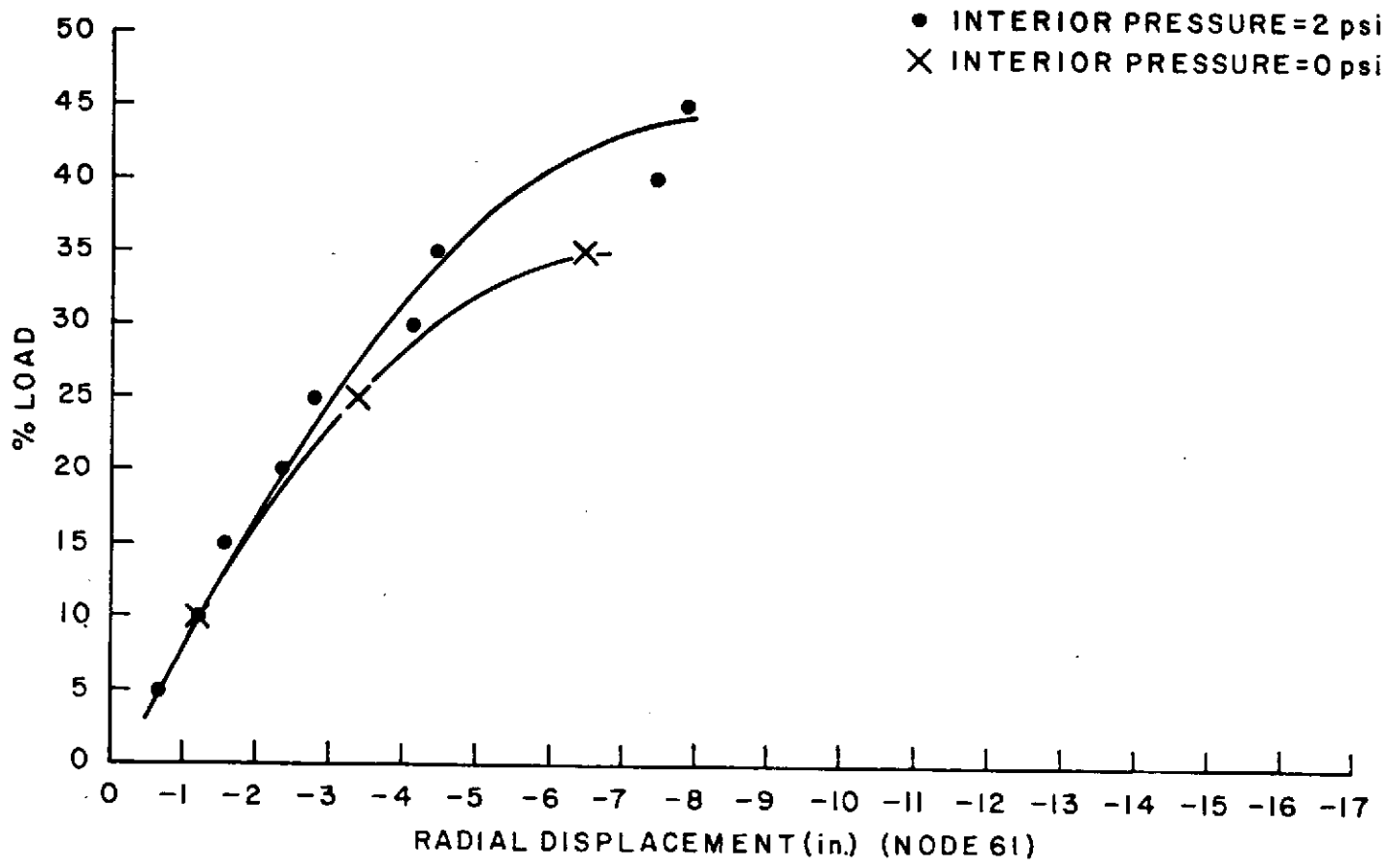
• INTERIOR PRESSURE=2 psi
X INTERIOR PRESSURE=0 psi
% LOAD
50
45
40
35
30
25
20
15
10
5
0
0 -1 -2 -3 -4 -5 -6 -7 -8 -9 -10 -11 -12 -13 -14 -15 -16 -17
RADIAL DISPLACEMENT (in.) (NODE 61)

FIG.6.4

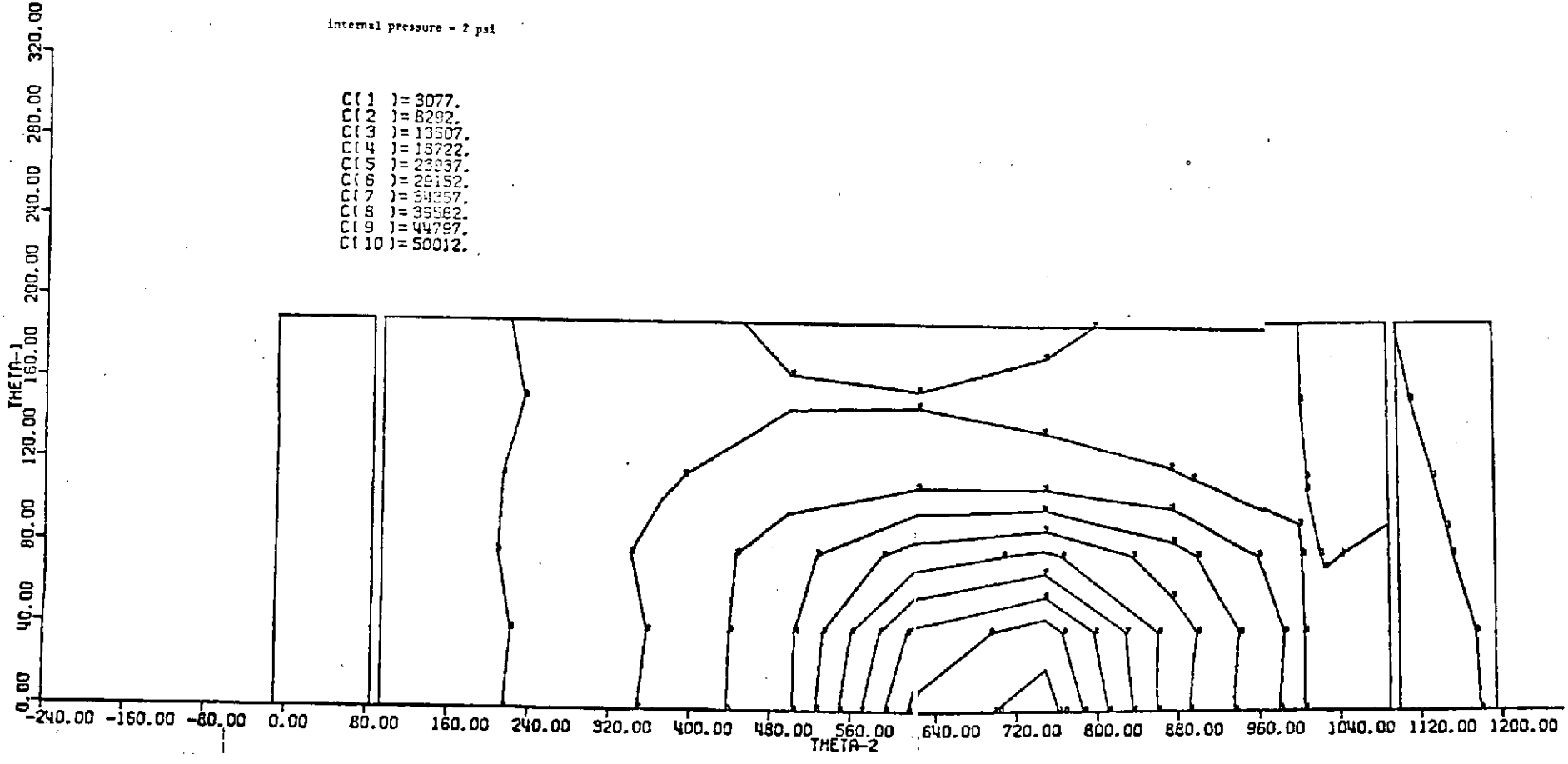

FIG.6.5 EQUIVALENT STRESS PLOT ON TOP SURFACE

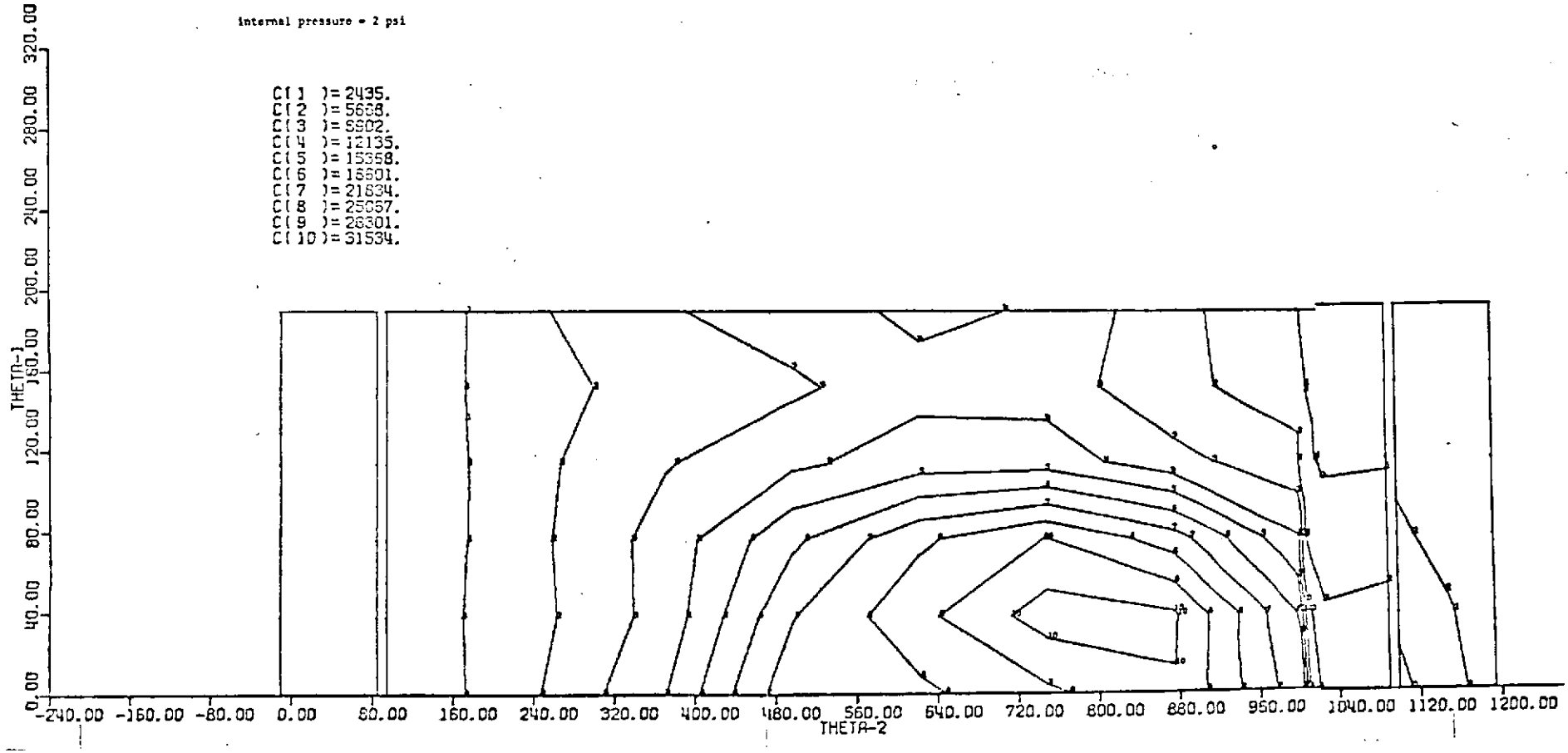

FIG. 6.6 EQUIVALENT STRESS PLOT ON BOTTOM SURFACE

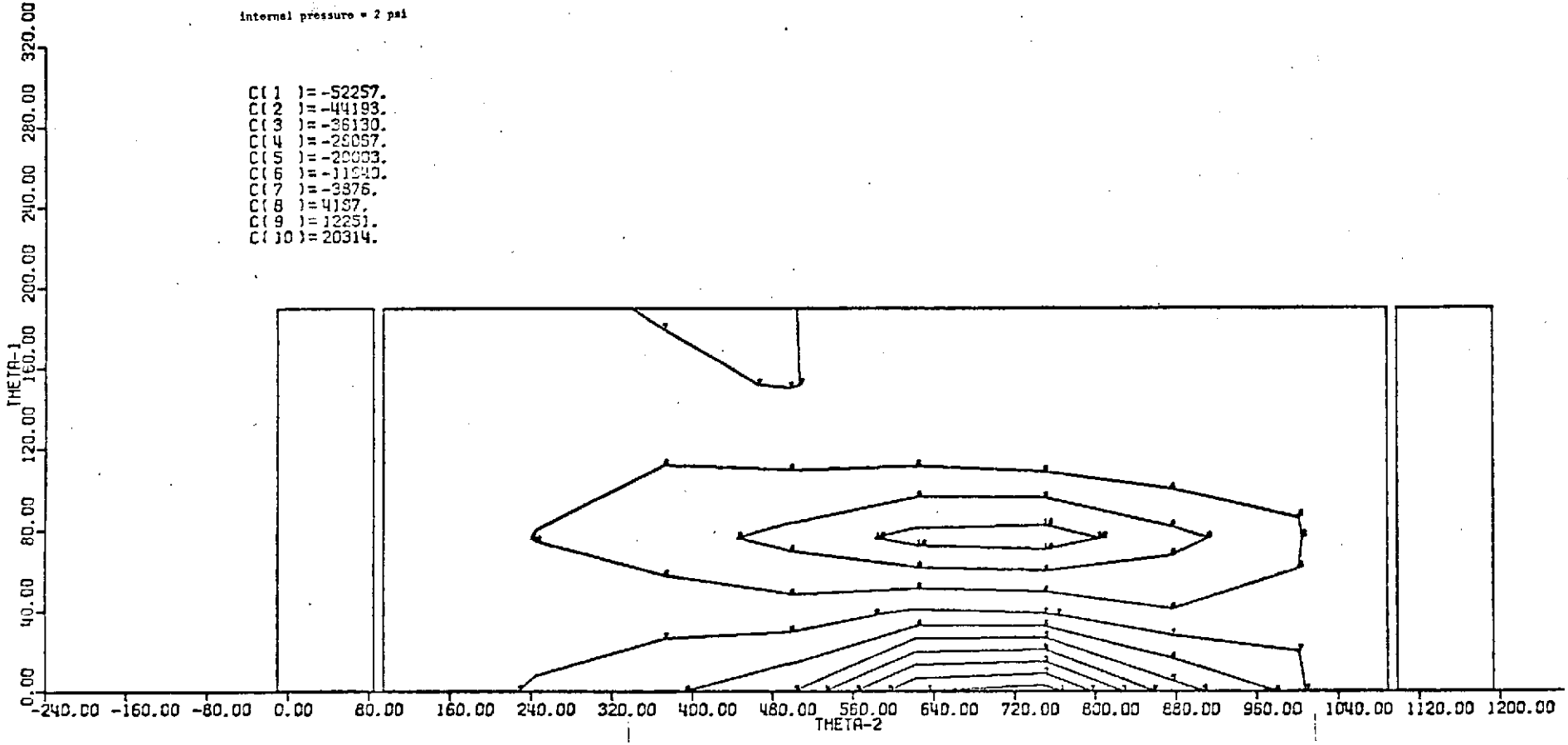

FIG. 6.7 EQUIVALENT STRESS PLOT ON TOP SURFACE

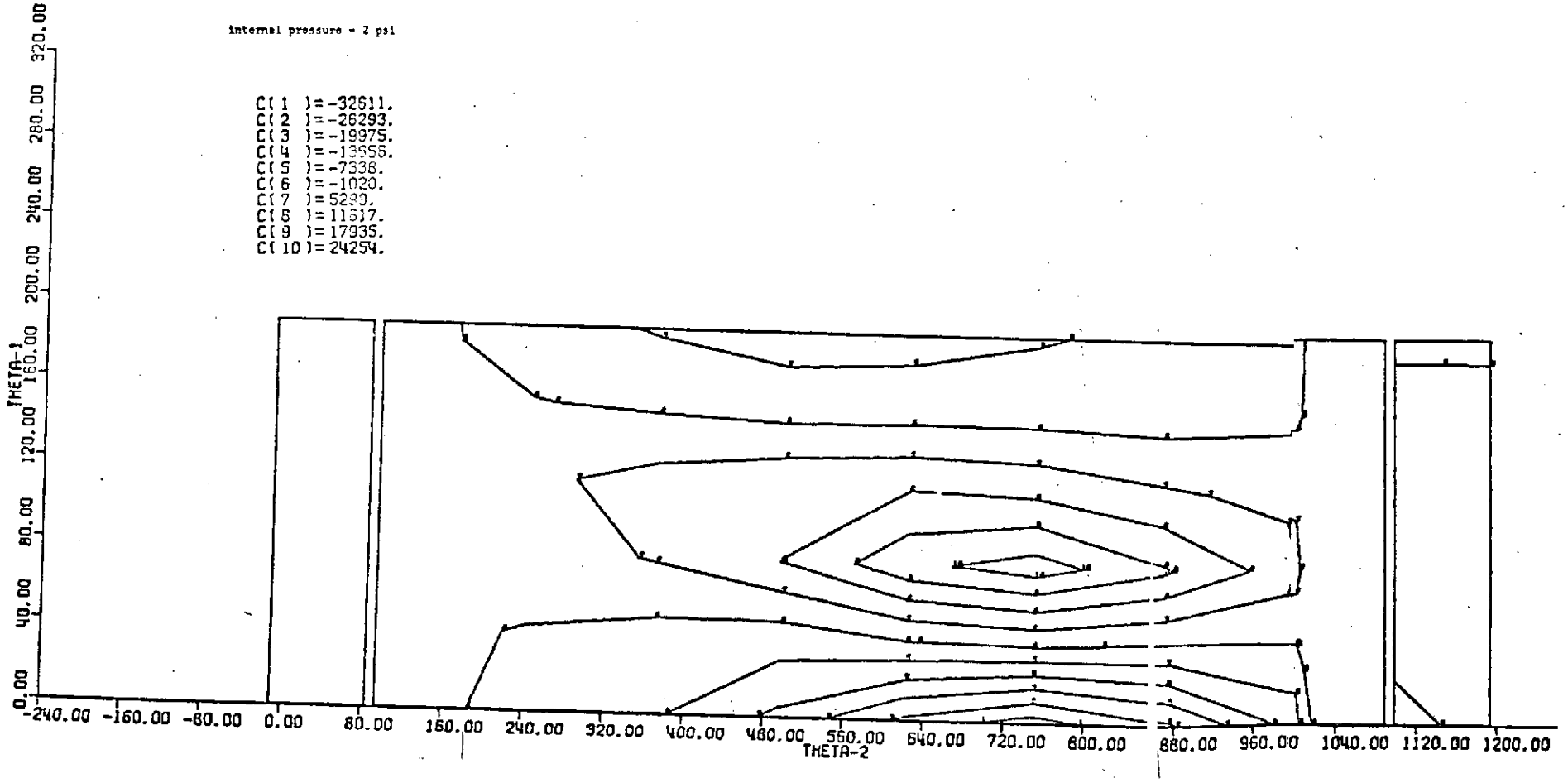

FIG.6.8 EQUIVALENT STRESS PLOT ON TOP SURFACE

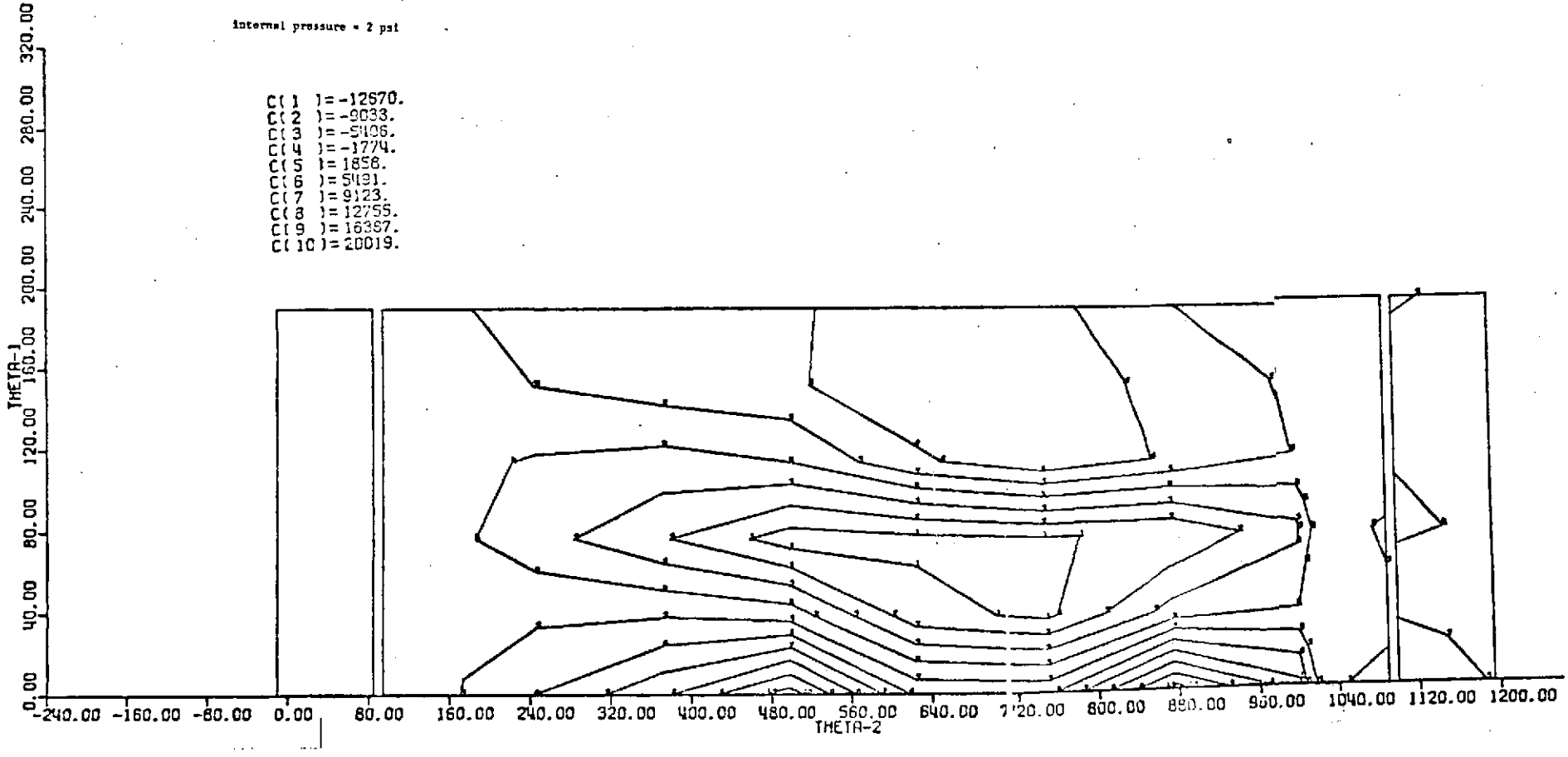

FIG. 6.9 EQUIVALENT STRESS PLOT ON BOTTOM SURFACE

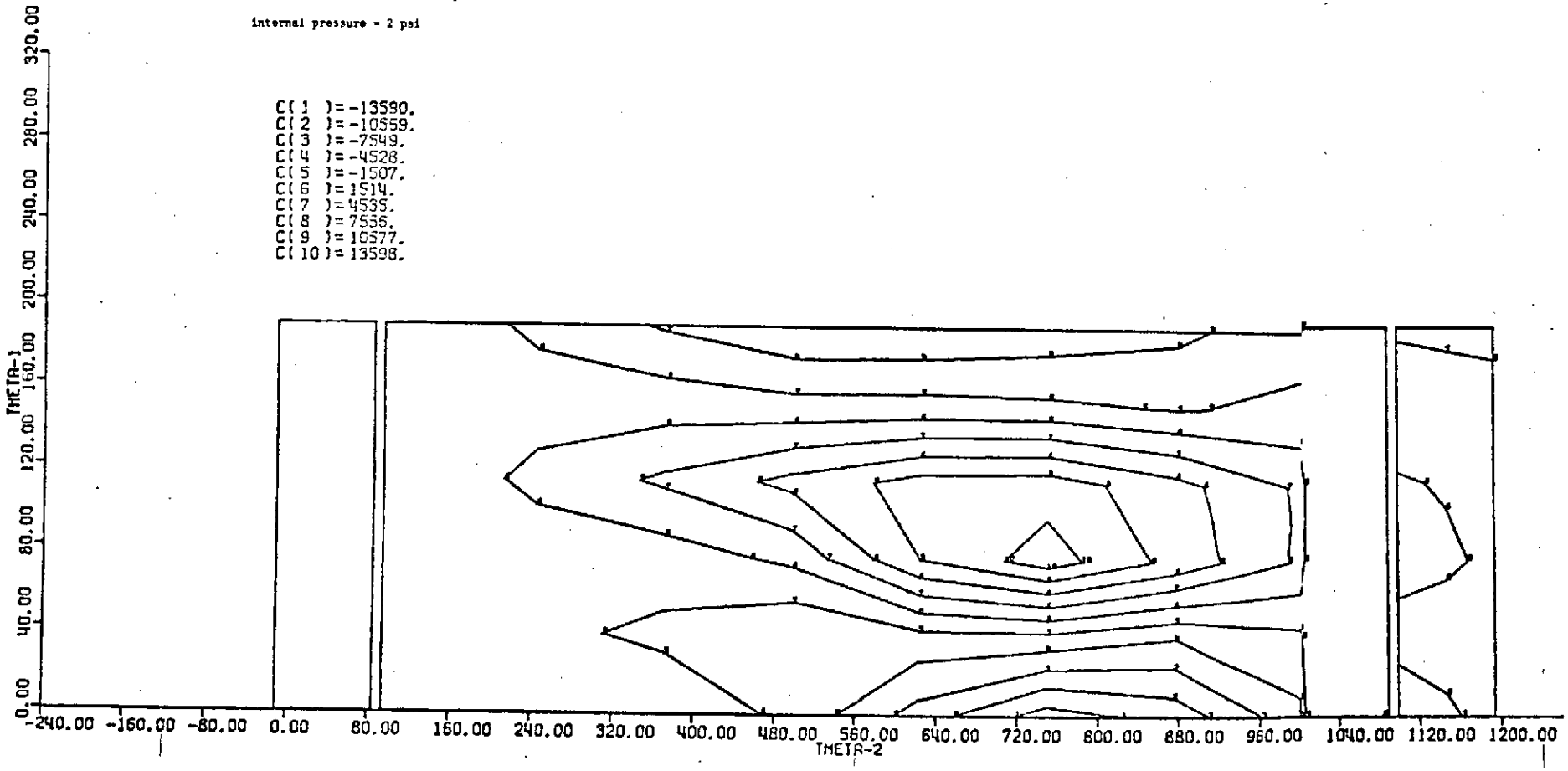

FIG. 6.10 EQUIVALENT STRESS PLOT ON BOTTOM SURFACE

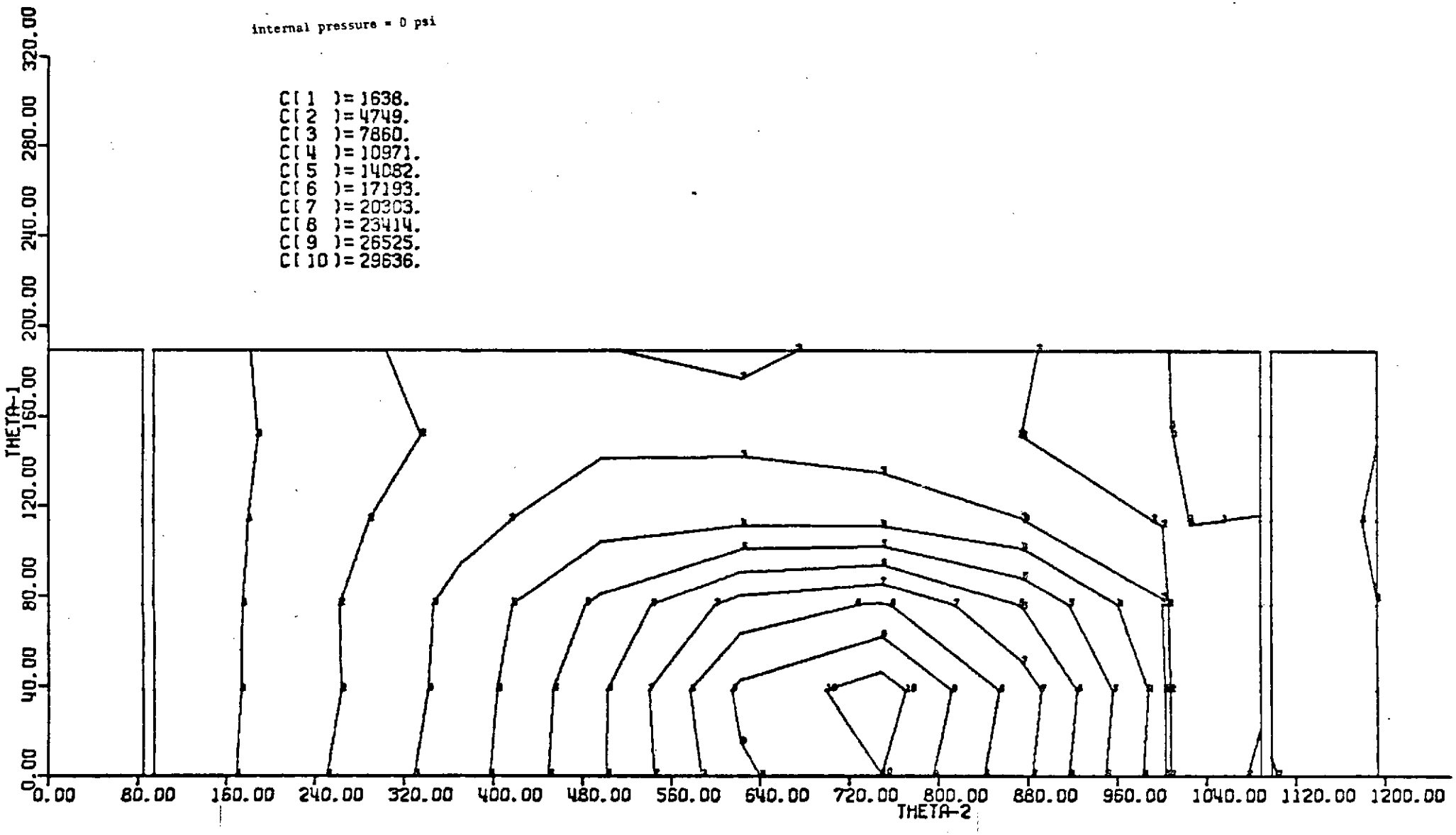

FIG. 6.11 EQUIVALENT STRESS PLOT ON TOP SURFACE

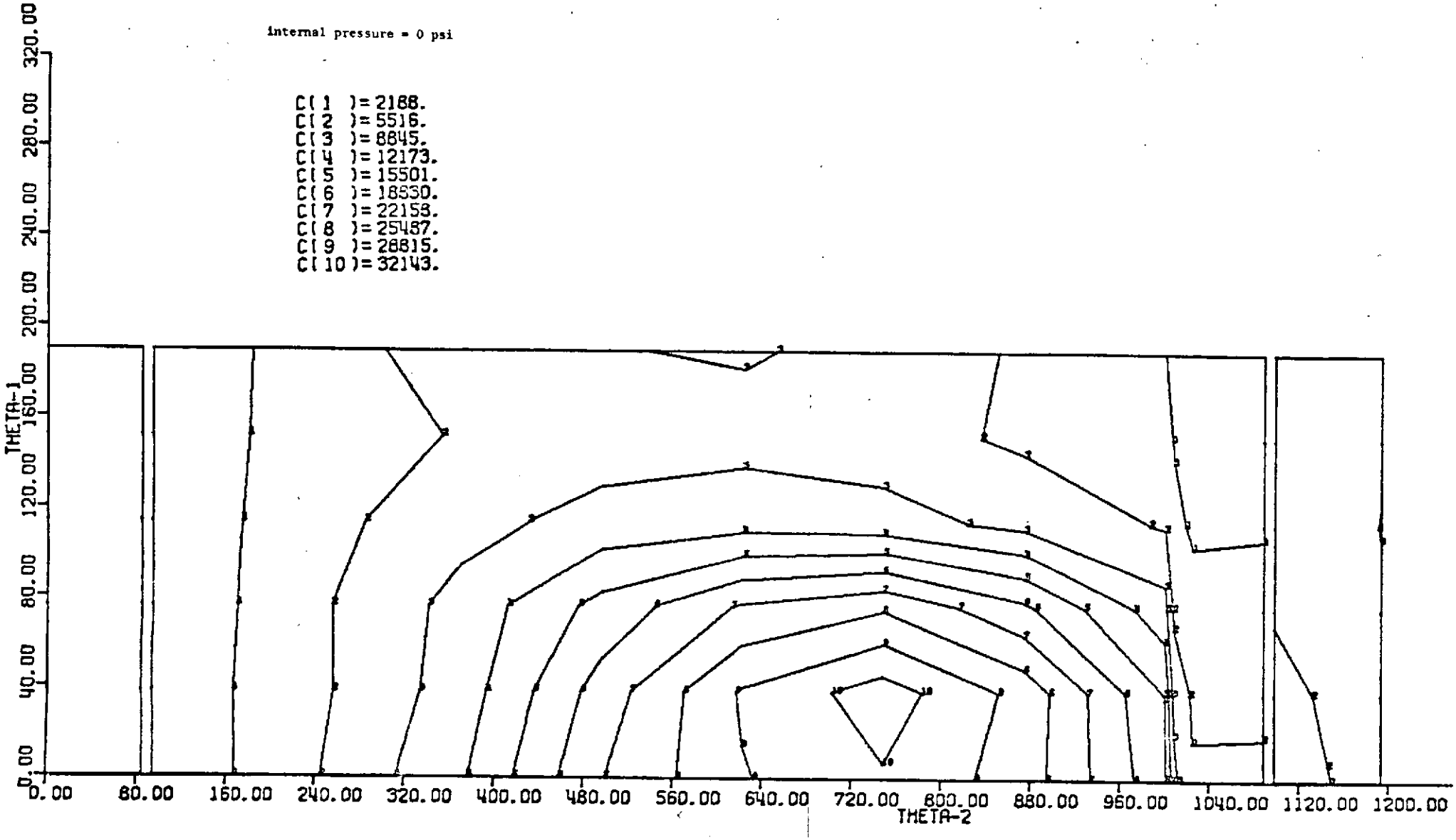

FIG. 6.12 EQUIVALENT STRESS PLOT ON BOTTOM SURFACE

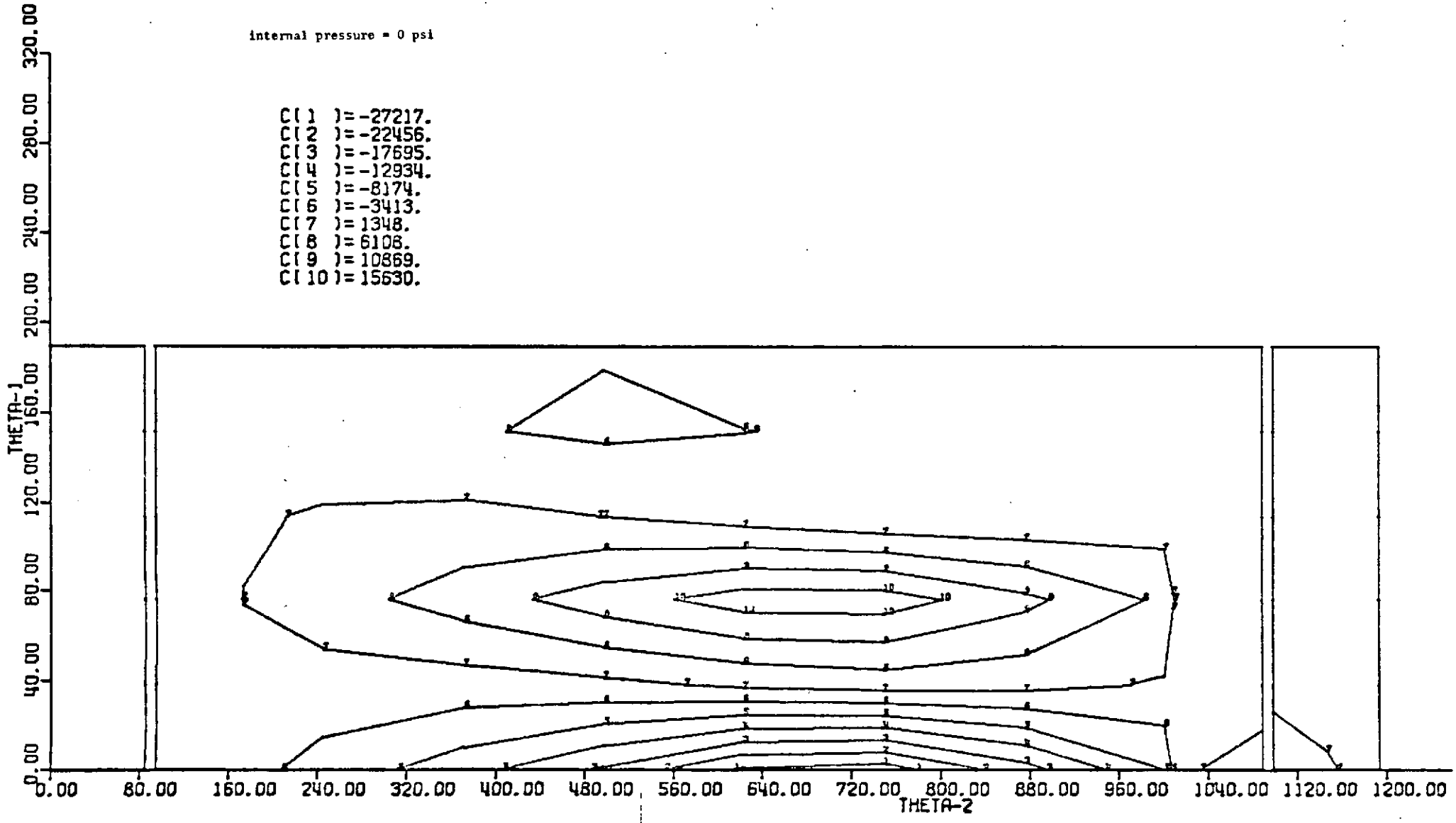

FIG.6.13 THETA I STRESS PLOT ON TOP SURFACE

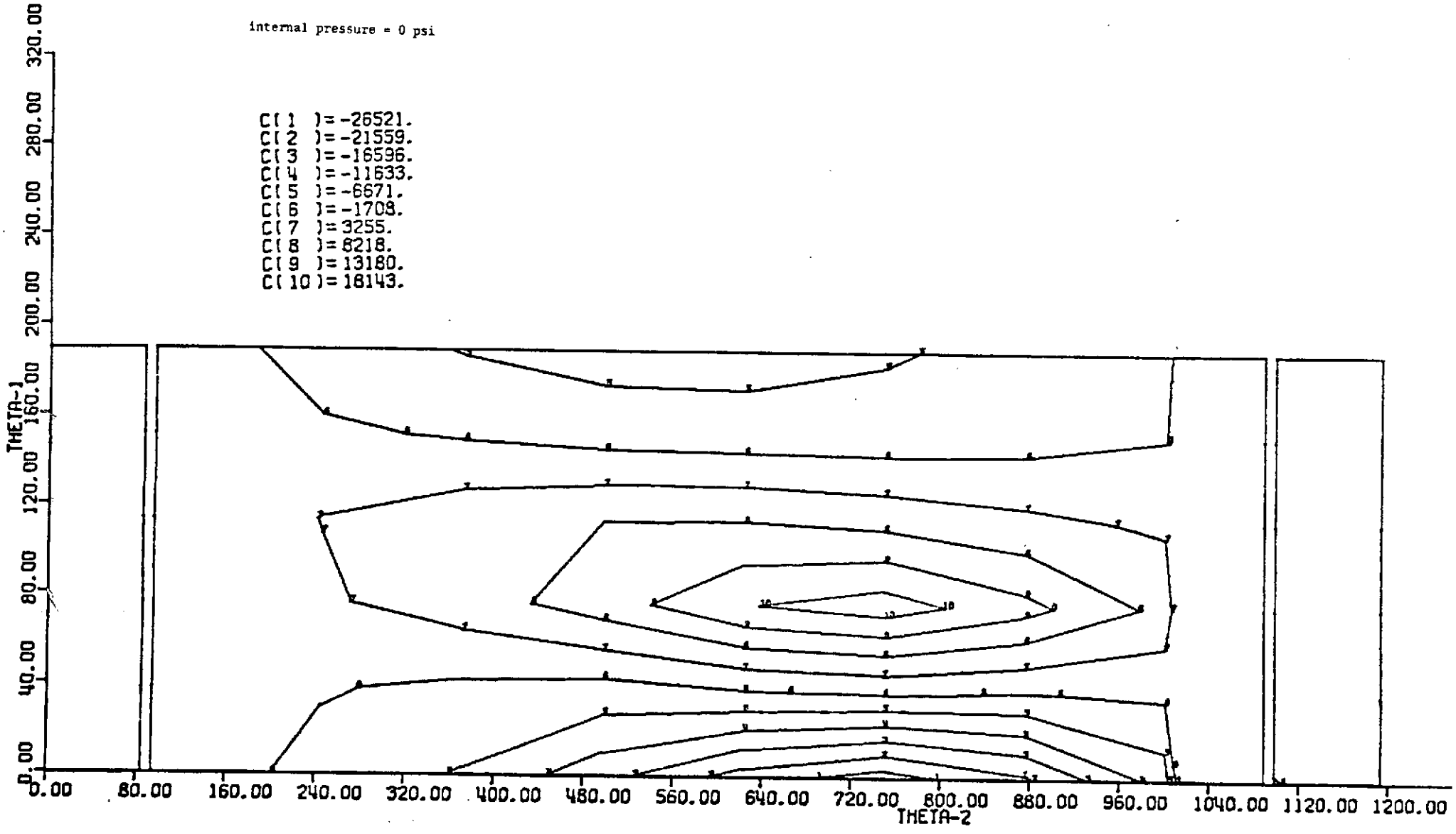

FIG. 6.14 THETA 2 STRESS PLOT ON TOP SURFACE

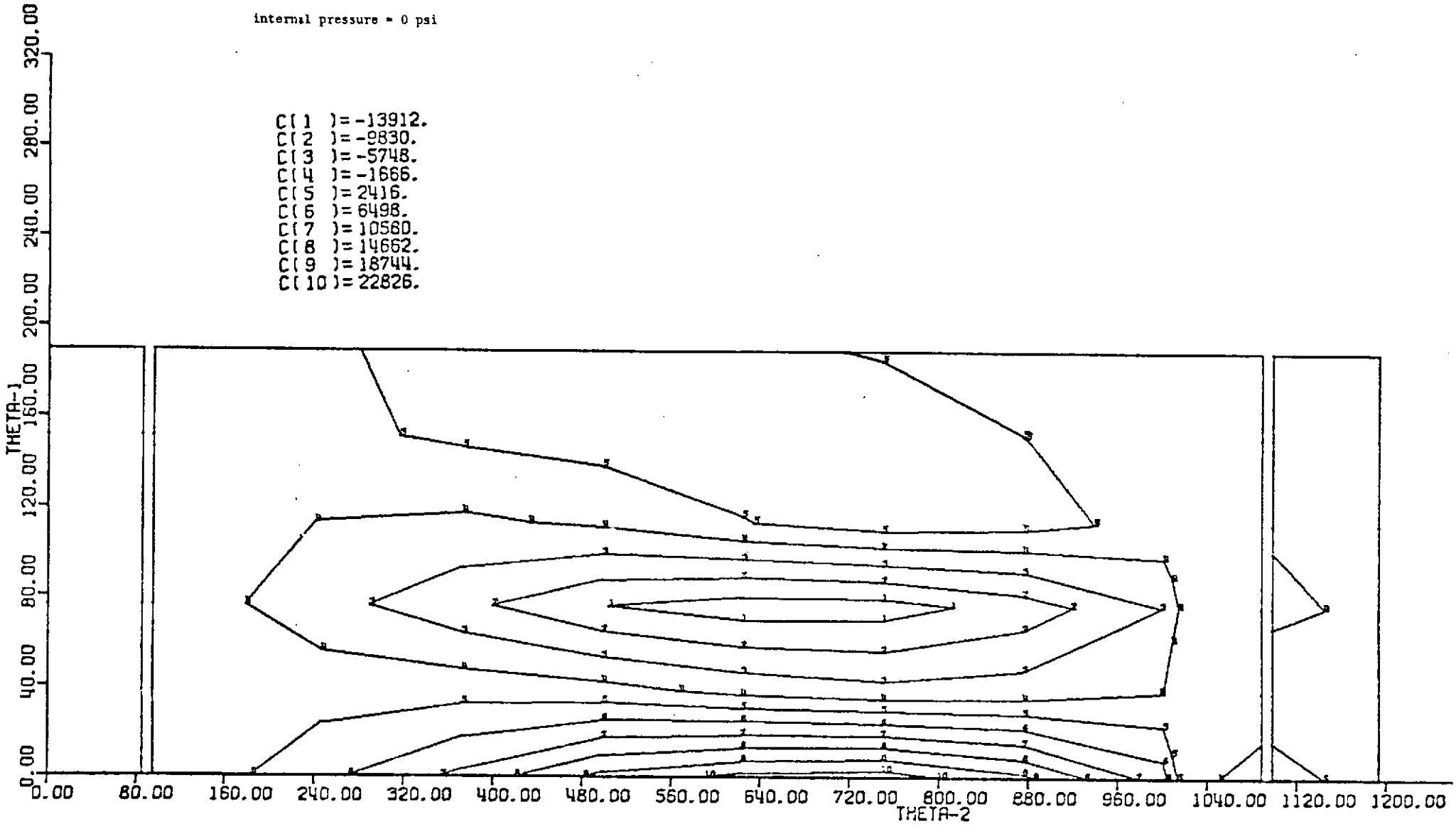

FIG. 6.15 THETA I STRESS PLOT ON BOTTOM SURFACE

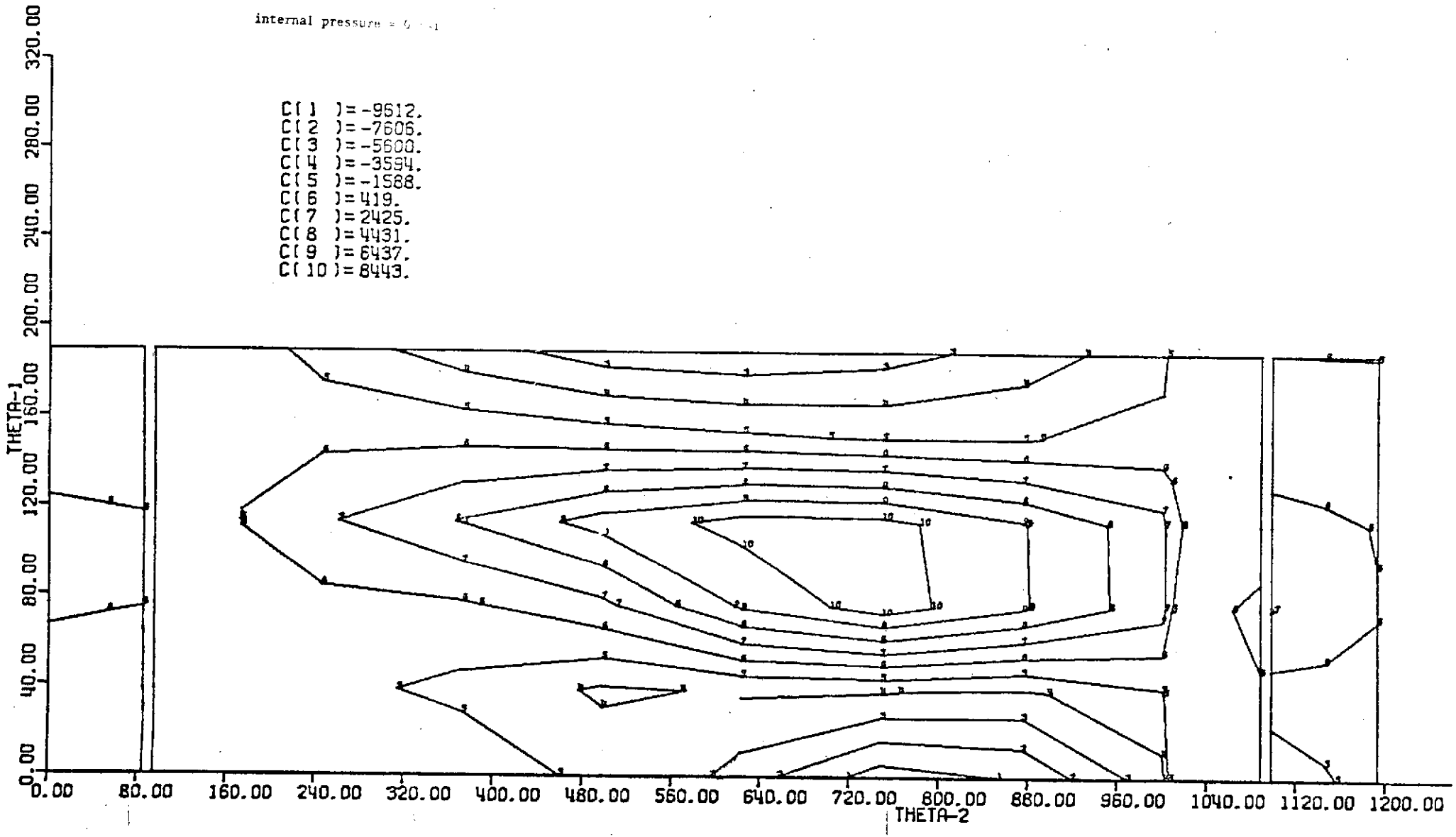

FIG. 6.16 THETA 2 STRESS PLOT ON BOTTOM SURFACE

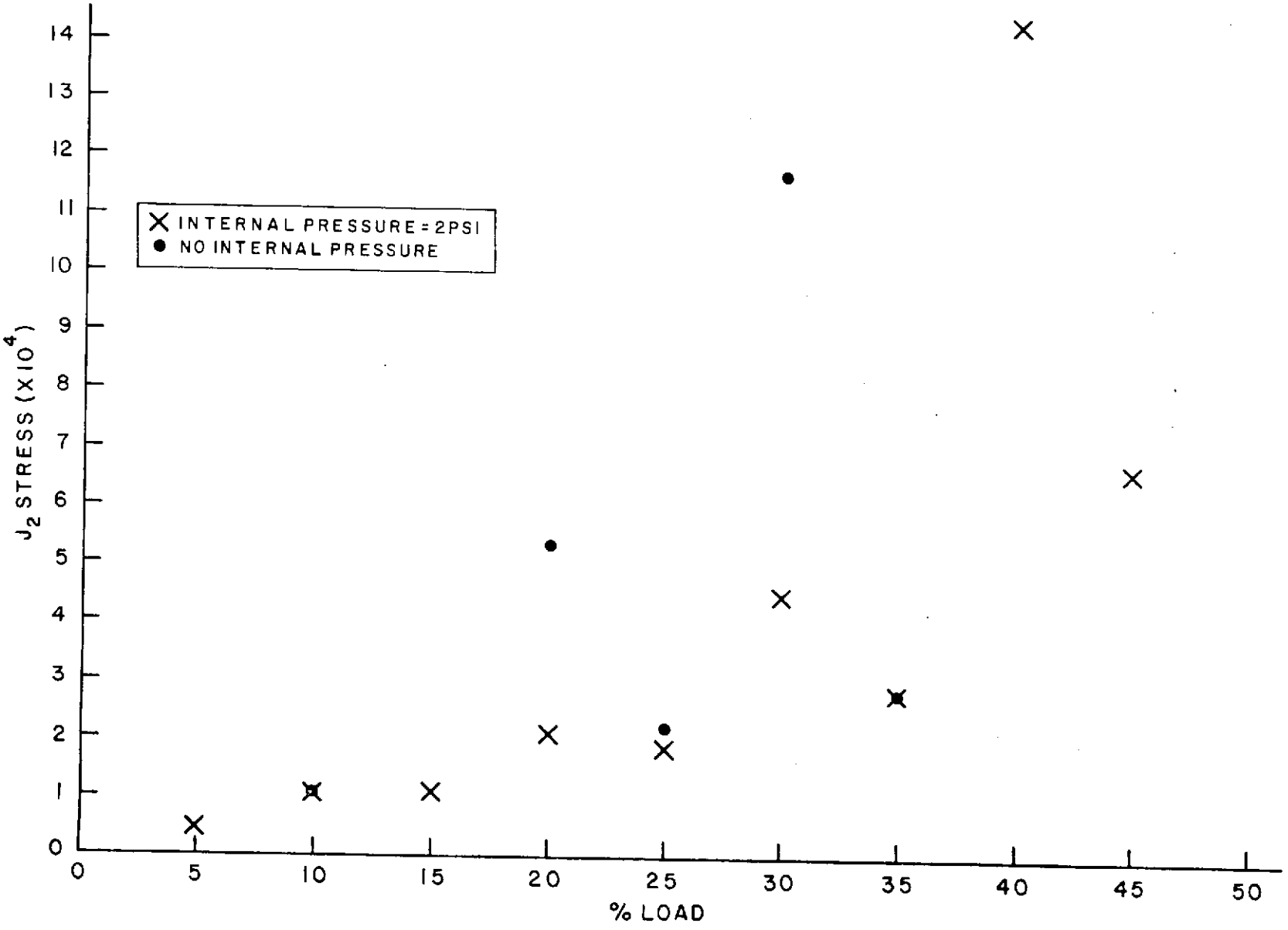

FIG. 6.17 J_2 STRESS IN ELEMENT 41

At this stage, new results from the drop test instrumentation resulted in a less severe pressure loading condition. The pressure was more localized. The analysis was repeated for this loading condition.

A non-linear, inertia loaded analysis of the same 120" casing geometry analyzed in previous work has been performed. The pressure distribution differed from that assumed previously, with a localized pressure spike of 55 psi at Z=450". Some comparisons with previous analyses using the same geometry but the previous pressure distribution are made in this section.

MODEL

The modelling is of the 120" casing described in previous reports. The quadrilateral shell element was used to allow modelling with a coarser mesh at a small penalty in solution accuracy. The geometric model used for the present analysis is shown in Figure 5.1 and the mesh is shown in Figure 5.1A.

LOADING

The mechanical loading distribution used for this analysis is shown on Figures 7.1 and 7.2. Note the radical difference between this pressure loading and the pressure loadings used in previous analyses. The total applied pressure is about 2.5 times less in this analysis than that used previously.

The above mechanical loading was reacted by an interia loading as previously derived. For this analysis, the necessary constants have the following values:

$$P_x = -9.2288 \times 10^4 \text{ lb}$$

$$z_c P_x = -4.66293 \times 10^7 \text{ lb-in}$$

$$V = 7.06297 \times 10^4 \text{ in}^3$$

$$J_y = 3.51284 \times 10^7 \text{ in}^4$$

$$I_y = 2.40335 \times 10^{10} \text{ in}^5$$

where

P_x = net external force in x direction

z_c = center of influence of external pressure

V = Volume of shell

J_y = 1st moment of area of shell about y axis

I_y = 2nd moment of area of shell about y axis

RESULTS

a) Displacements

The full load deformation mode (Figures 7.3 and 7.4) shows peak displacement occurring more toward the forward end as compared with the previous load distribution: at Z = 480" in the current analysis, and Z = 750" with the previous load case. Surprisingly, although the pressure spike is considerably more localized in this analysis, the deformation mode does not appear to be correspondingly localized. There is a possibility that the mesh used for this analysis was excessively coarse for such a loading: no convergence tests were performed for the new pressure distribution, since it was felt that, based on previous experience with such elements, this mesh could capture sharp strain gradients. Nevertheless, convergence tests would be of value.

Figure 7.5 shows peak x-direction displacement on the load symmetry plane plotted as a function of full load fraction. The linearity of the response is clearly evident in this plot, the initial slope change being attributed to the constant internal pressure. Peak displacement was 3.73", compared to about 7.5" in the previous analysis at 45% of that prescribed full load. This difference is not surprising, since little localization was observed, and the net load in the present case is 2.5 times less than that in section 6.

b) Stress

Maximum stresses occur at the element integration point closest to the load spike and are as follows:

Equivalent J_2 stress (psi)	33000
Hoop stress (psi)	22000
Axial stress (psi)	16000

The various stress components calculated are on the inside and outside of the casing contoured on Figures 7.6-7.11. Note especially in the two plots of equivalent J_2 stress (Figures 7.6 and 7.7) the similar stress pattern with the maximum stress occurring directly beneath the peak pressure, and with high stress gradients in that neighborhood.

Compared with previous analyses stresses are overall much lower again because the pressure distribution used for this analysis is less severe than those used in previous analyses.

CONCLUSIONS

The present analysis suggests that there is no likelihood of geometric or material failure under the prescribed loading pattern and magnitude. This is in sharp contrast to the previously analyzed load cases (where the same finite

element model was used) where even with the 2 psi internal pressure, geometric failure occurred at 45% of the prescribed load magnitude.

All analyses to date have been based on neglect of the stiffening effects of the casing segment joints. Certainly this may be regarded as a conservative assumption, so that a stiffened analysis of the current load case should not be necessary, unless load magnitudes are to be significantly increased.

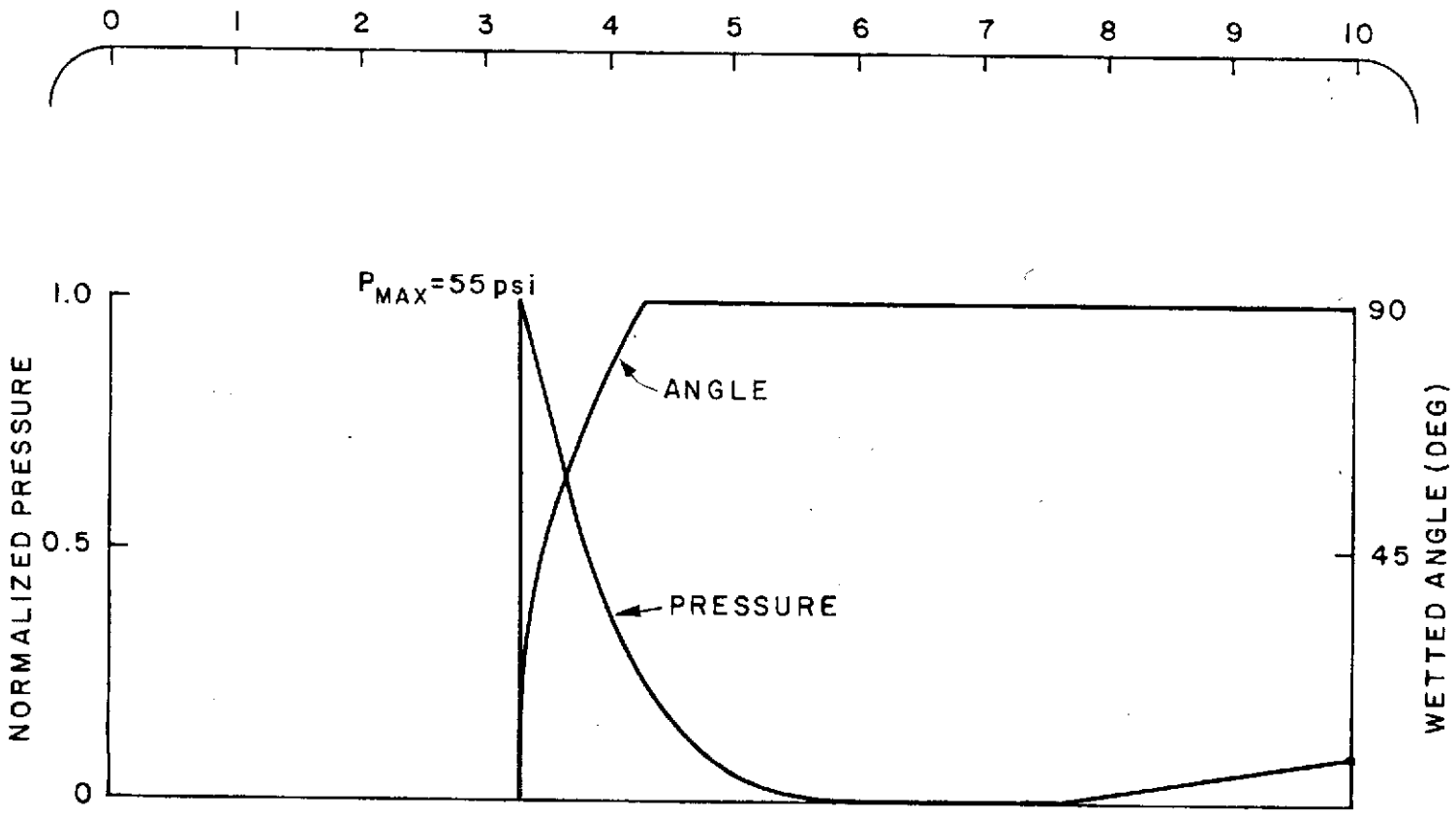

FIG.7.1 PRESSURE DISTRIBUTION

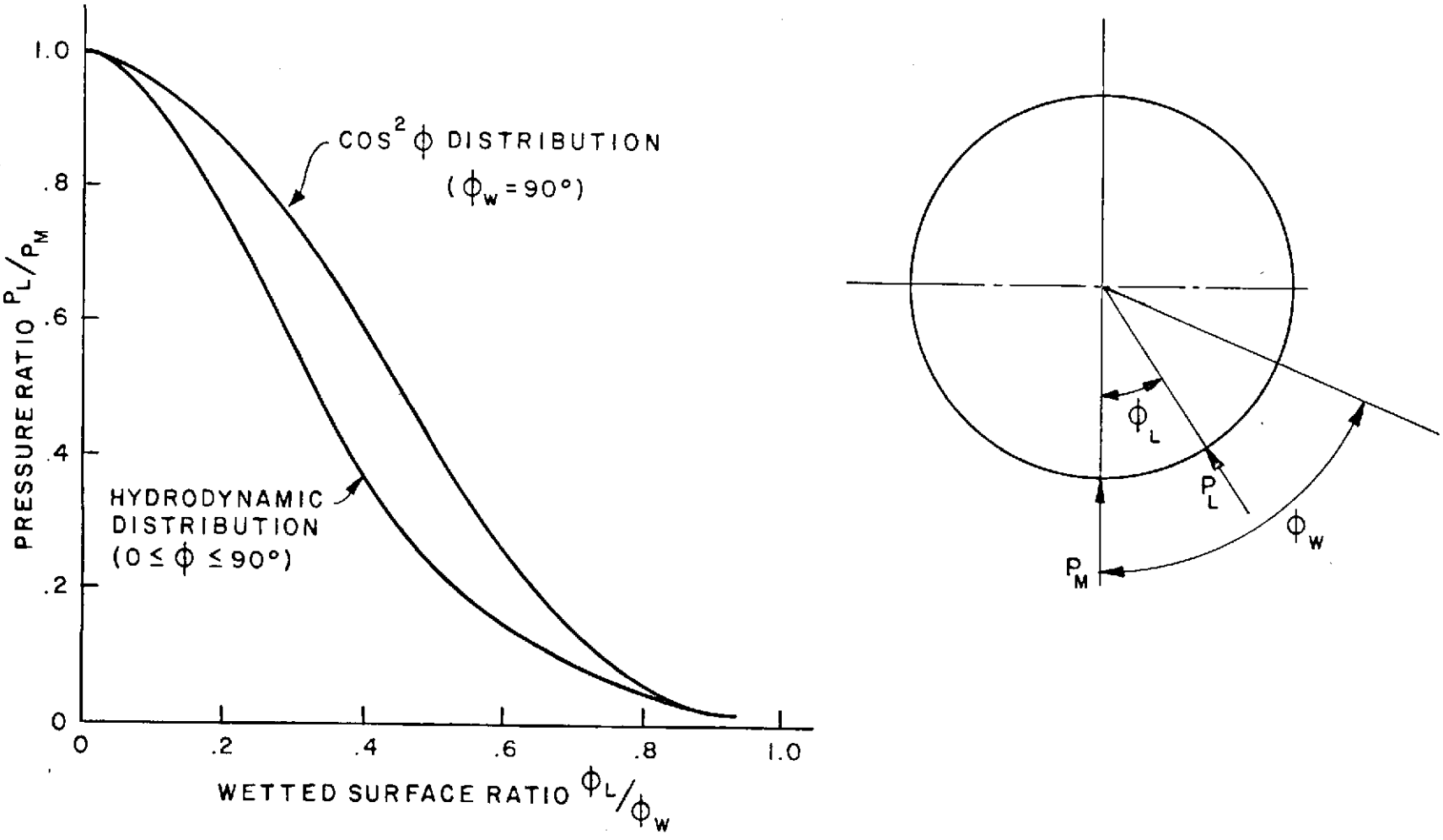

FIG. 7.2 NORMALIZED RADIAL SLAPDOWN PRESSURE DISTRIBUTIONS

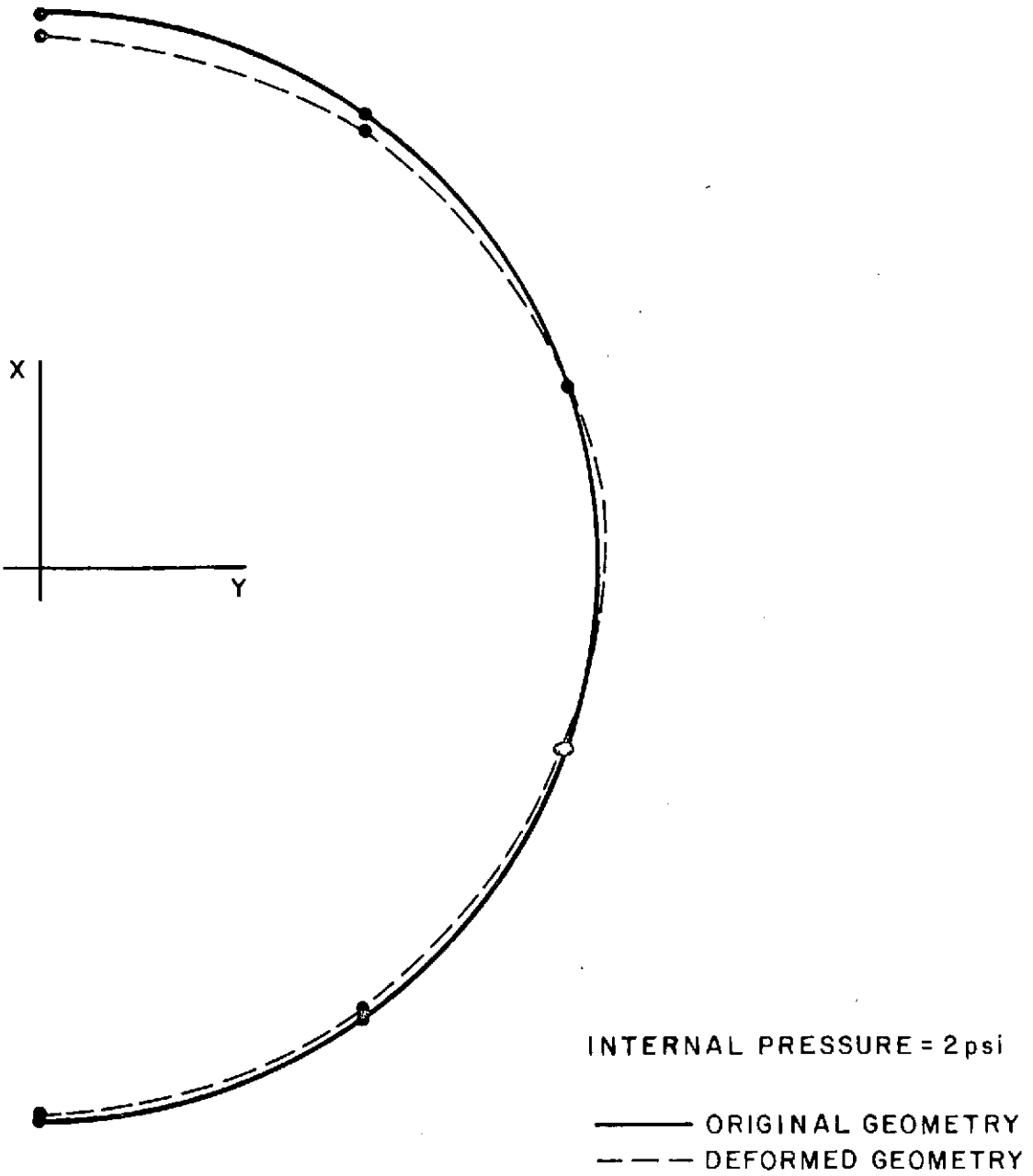

FIG. 7.3 DEFORMATION OF CROSS SECTION AT PEAK PRESSURE

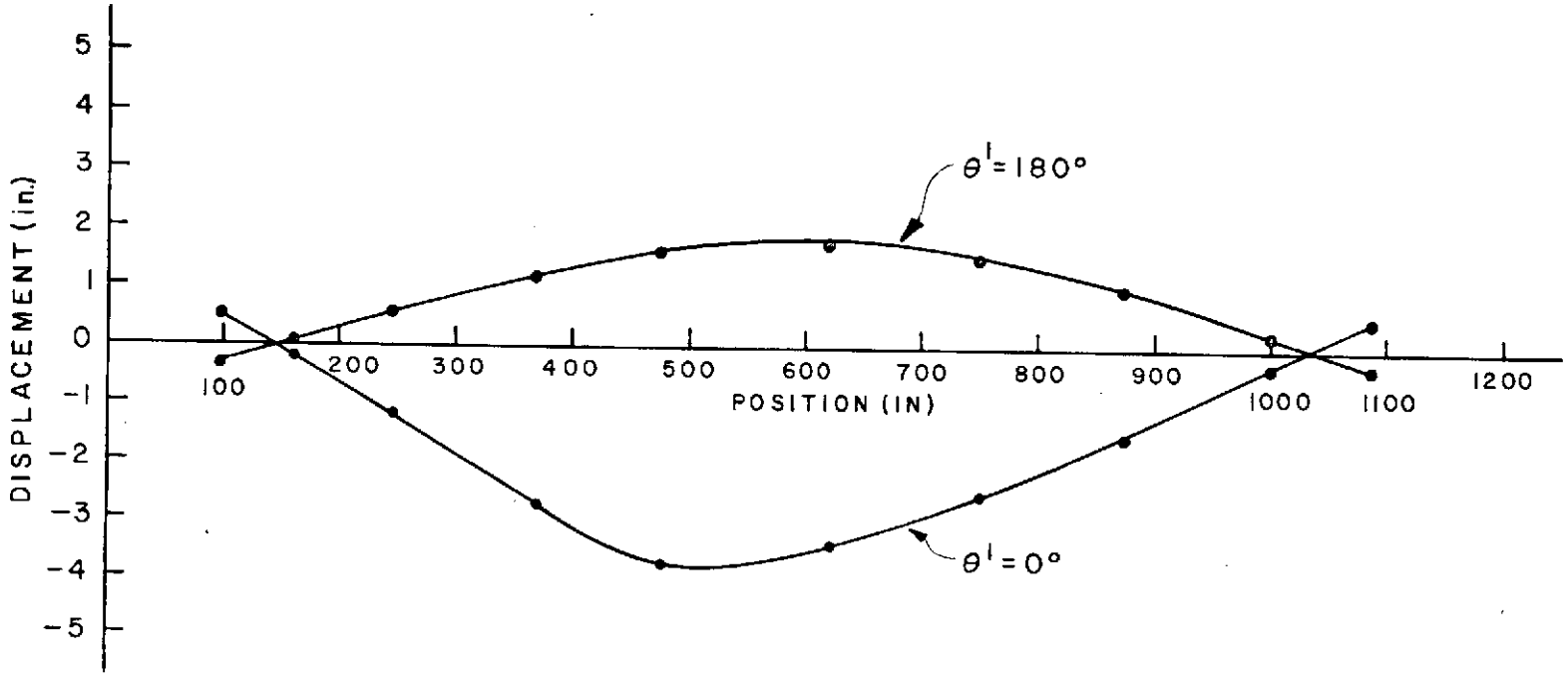

FIG. 7.4 RADIAL DISPLACEMENT

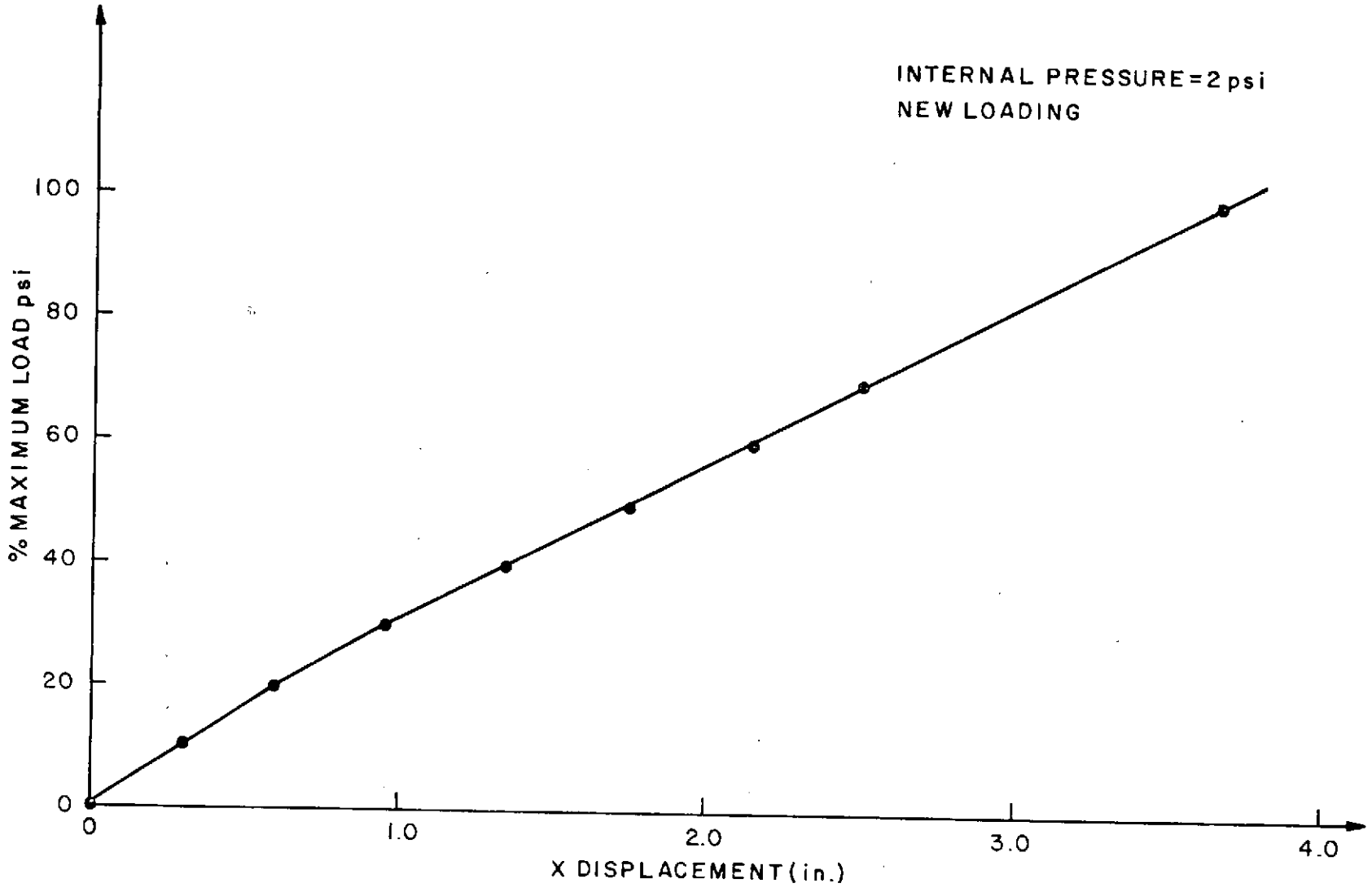
INTERNAL PRESSURE=2 psi
NEW LOADING
% MAXIMUM LOAD psi
100
80
60
40
20
0
0
1.0
2.0
3.0
4.0
X DISPLACEMENT (in.)

FIG. 7.5

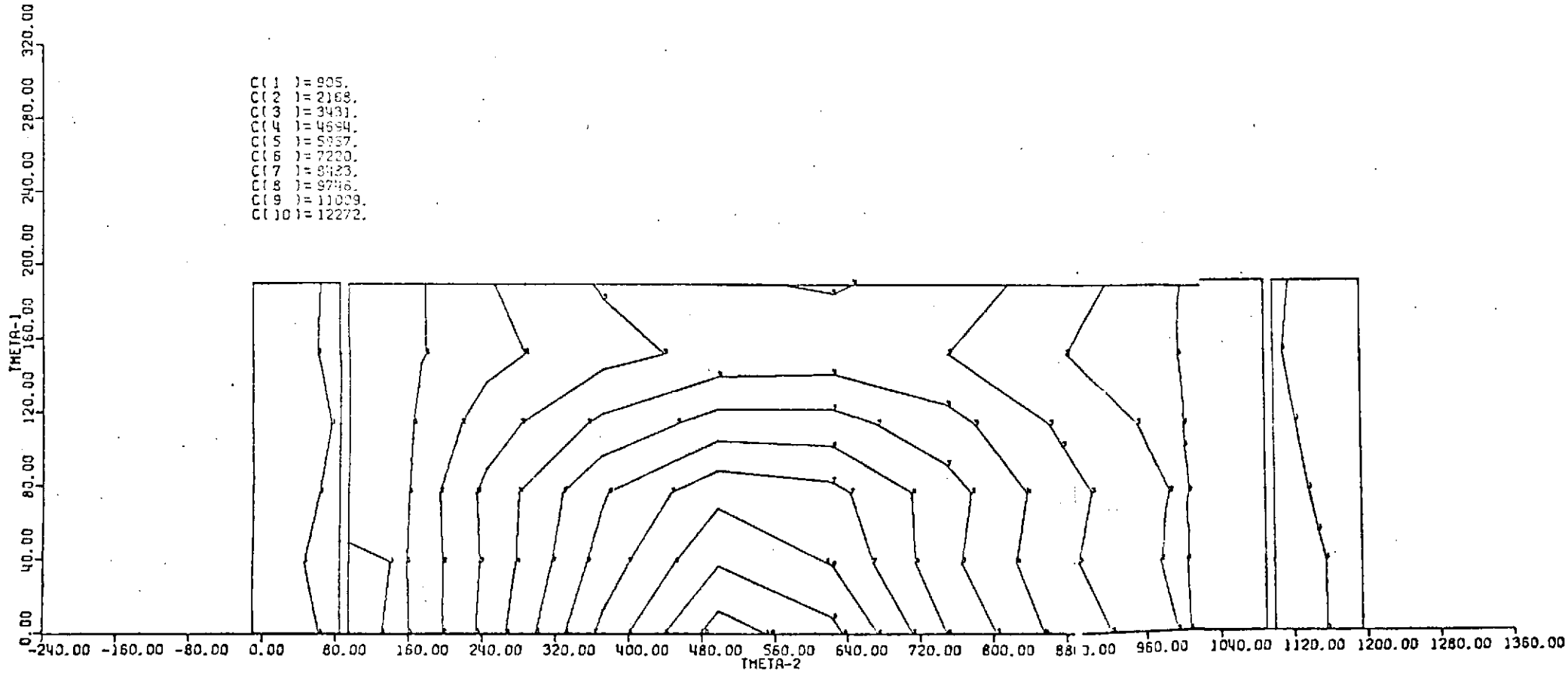

FIG. 7.6 EQUIVALENT STRESS PLOT ON TOP SURFACE

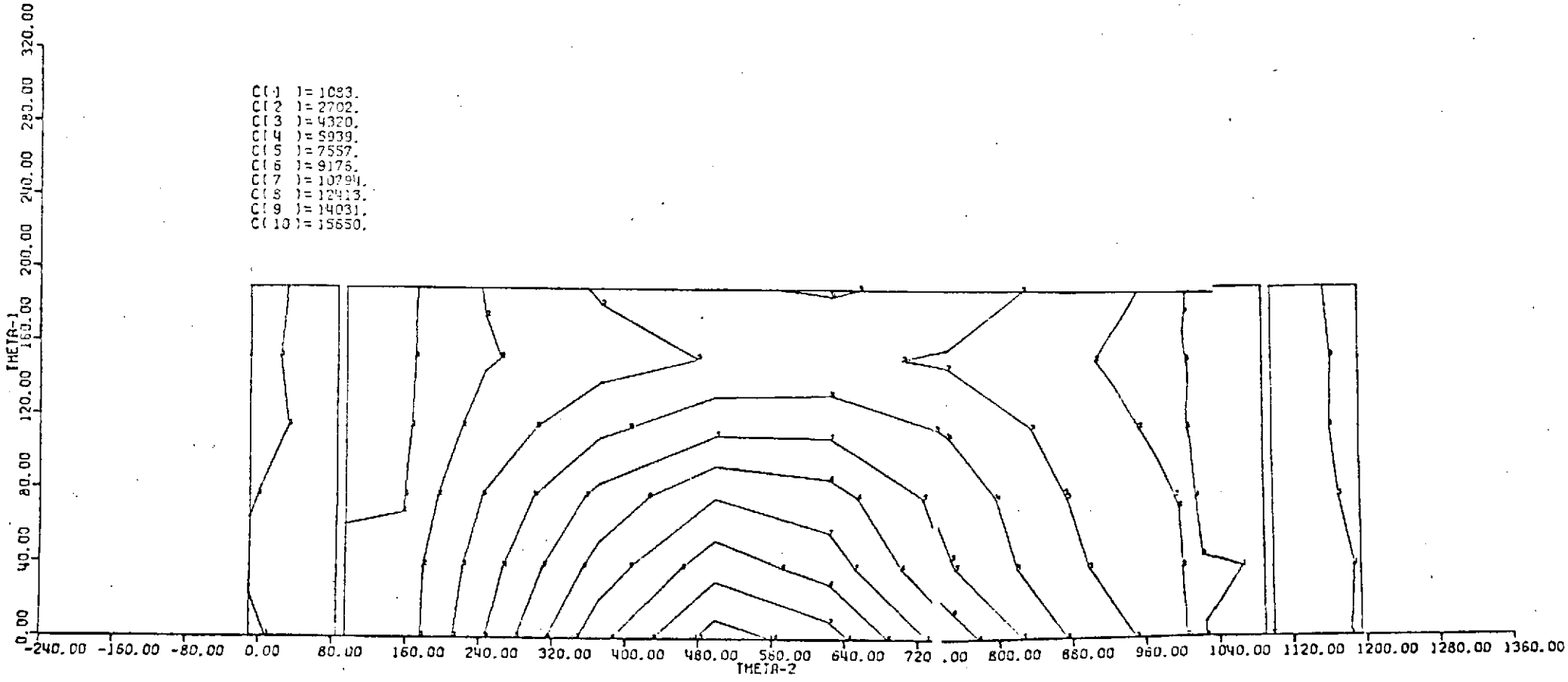

FIG. 7.7 EQUIVALENT STRESS PLOT ON BOTTOM SURFACE

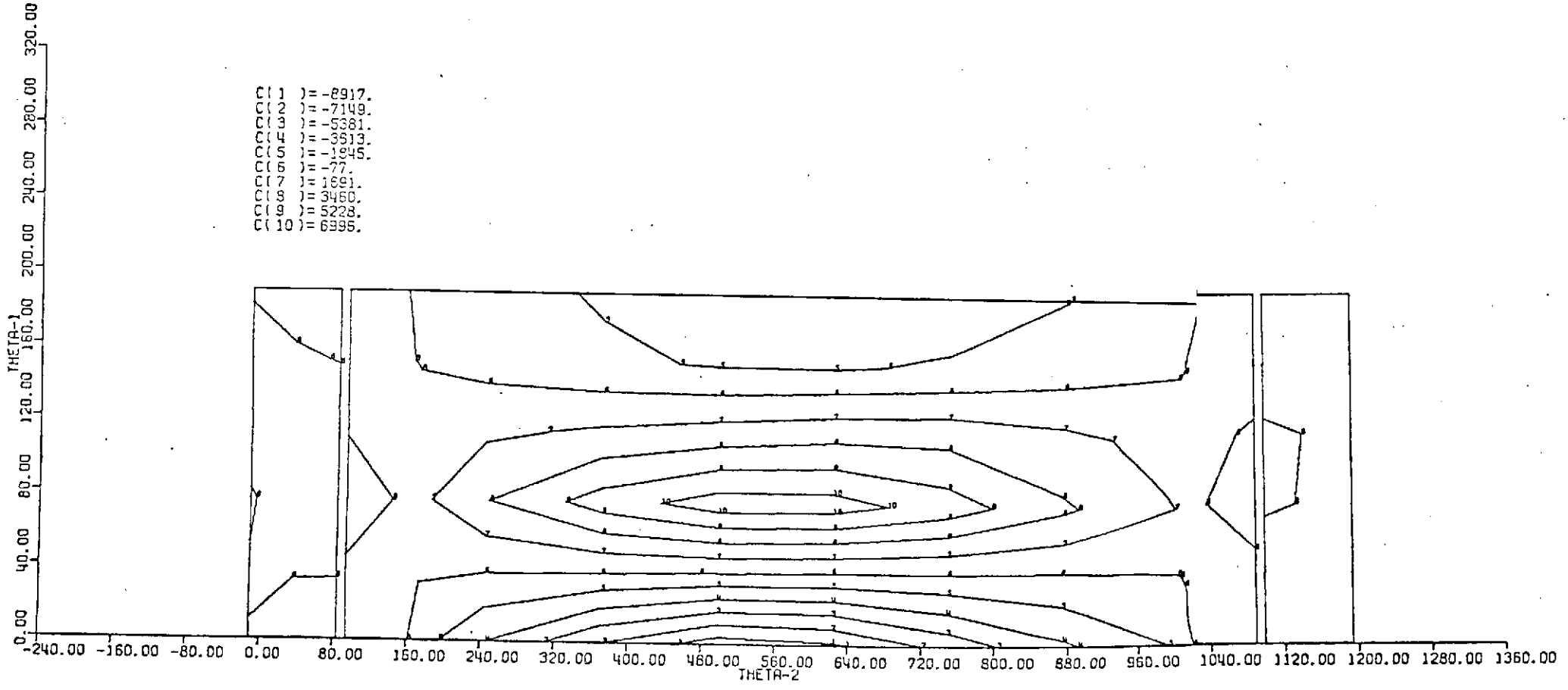

FIG. 7.8 THETA I STRESS PLOT ON TOP SURFACE

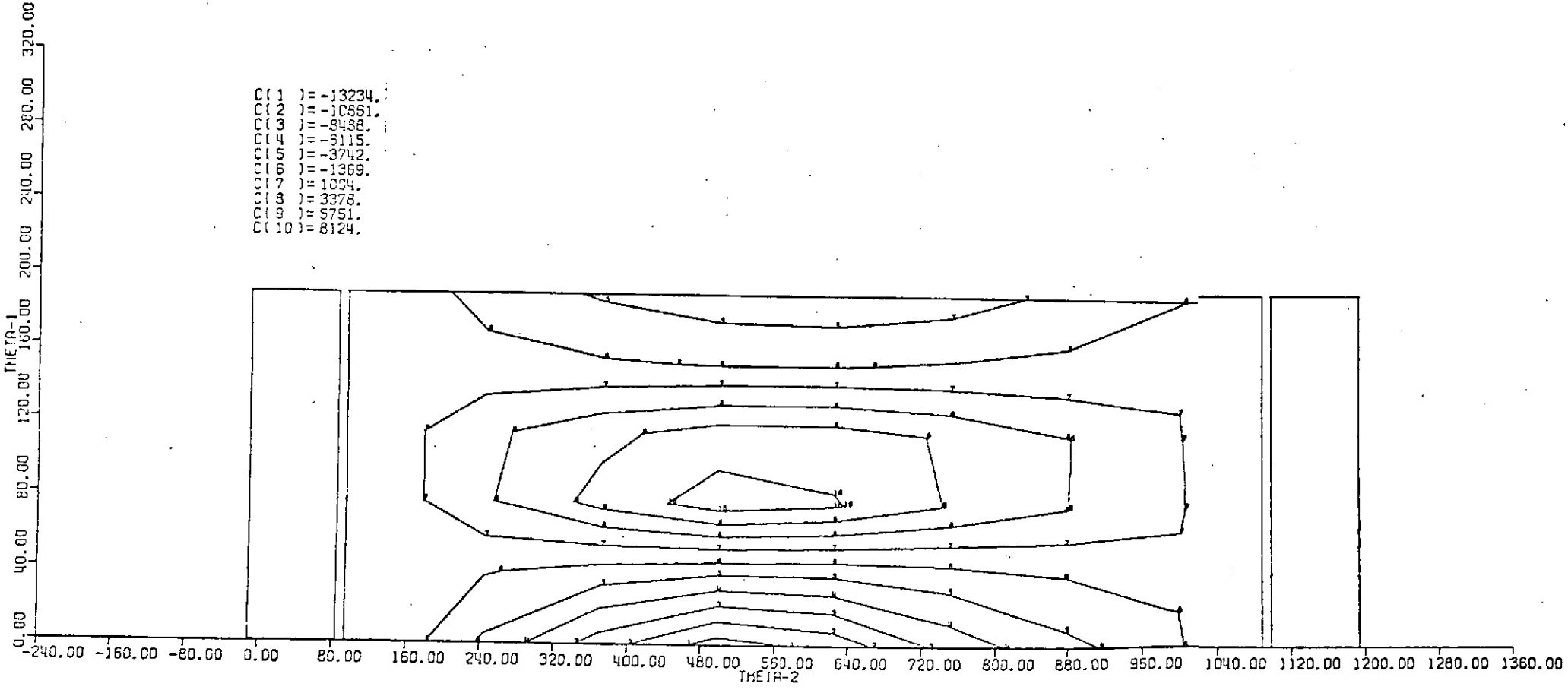

FIG. 7.9 THETA 2 STRESS PLOT ON TOP SURFACE

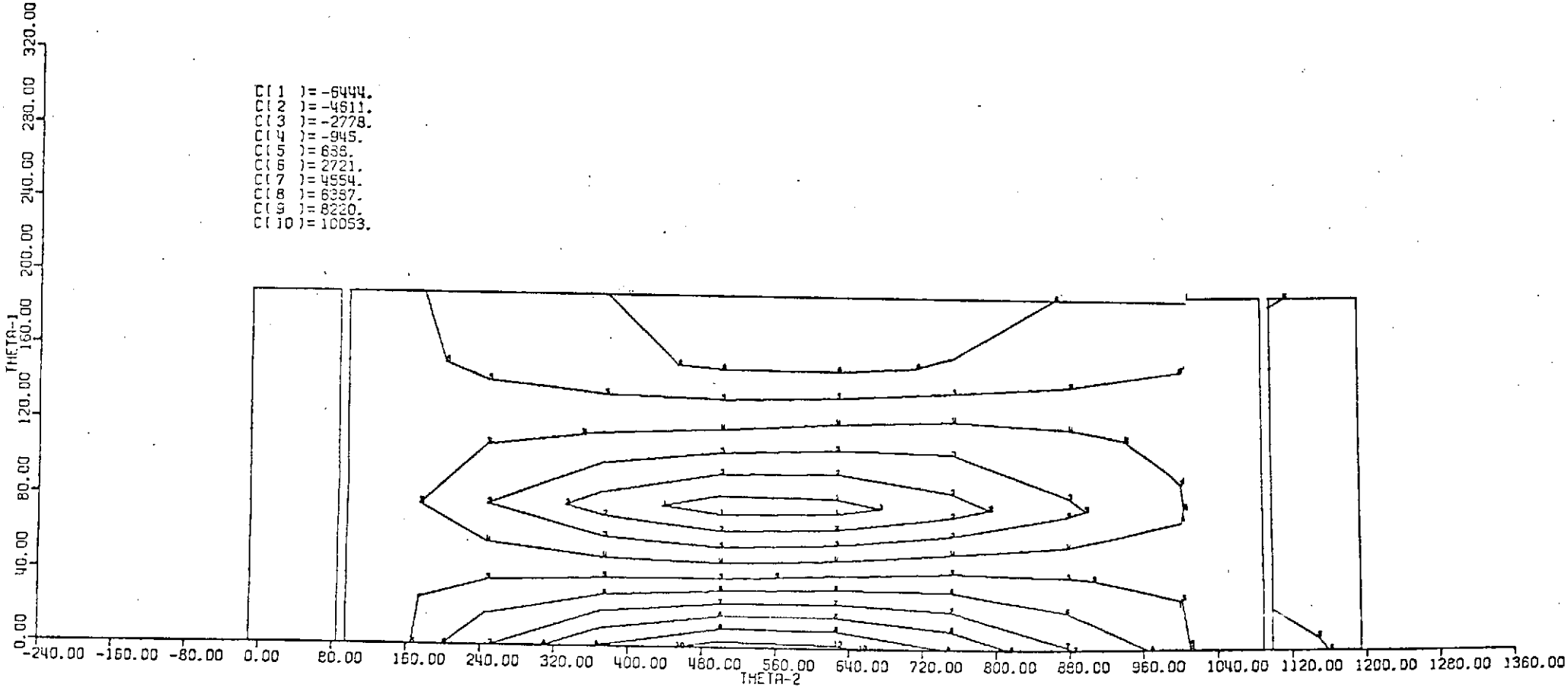

FIG. 7.10 THETA I STRESS PLOT ON BOTTOM SURFACE

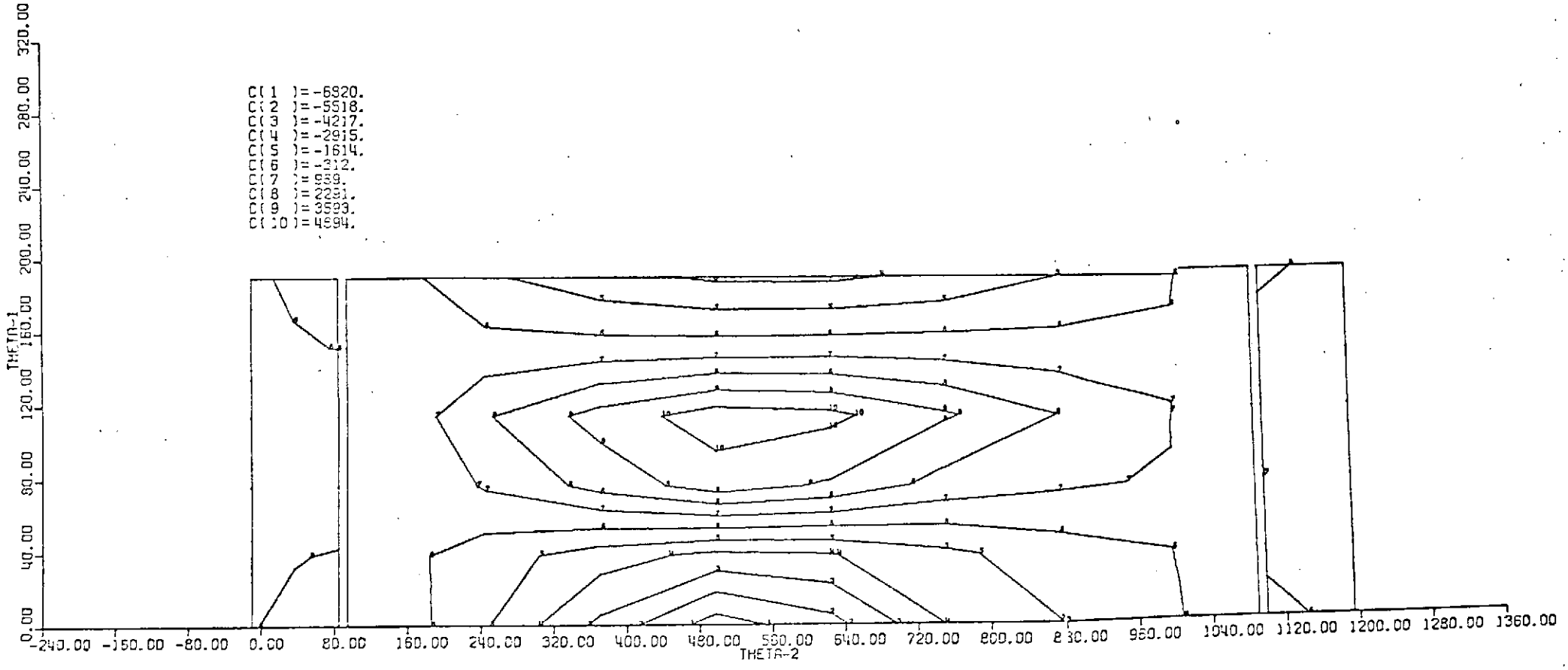

FIG. 7.11 THETA 2 STRESS PLOT ON BOTTOM SURFACE

From the results of the earlier analysis it may be concluded that the doubly curved triangular shell elements are not suitable for analysis of very flexible shell structures with small thickness to diameter ratios such as the rocket motor casings analyzed here.

The quadrilateral doubly curved shell elements were found to be much better than the triangular elements and were flexible enough for analysis of the current problems. The non-linear results using the original tentative loadings on the structure predicted that the structure would fail in service with a 35% application of full load. It was found that an internal pressure of 2 psi provided an extra load bearing capacity of 10%. It would be useful to show that the effect of this internal pressurization varies linearly with pressure.

The analysis with the more accurate load conditions show no signs of non-linearity up to full load. It is thus concluded that the structure is safe for service under these loads. The linear results obtained here were in agreement with results obtained with NASTRAN and BOSOR. This gives further confidence to the use of analysis for design of such shells subjected to splash down loadings.

ACKNOWLEDGEMENTS

The authors are indebted to Major C. Crockett of NASA-MSC for useful discussions.

1. G. A. Dupuis, Application of Ritz's Method to Thin Elastic Shell Analysis, Brown University Engineering Dept. Report N00014-0008/1, July, 1970.

2. J. C. VerHague and R. H. Mallett, Evaluation of an Isoparametric Surface Finite Element with C^1 Continuity, to be published.

3. A. C. Scordelis and K. S. Lo, Computer Analysis of Cylindrical Shells, J. Am Concr. Inst., Vol. 61, 539-61, 1969.

4. G. Dupuis and J. J. Goel, Some Numerical Results in Finite Element Analysis of Thin Elastic Shells, Ecole Polytechnique Federale, Lausanne, Dept. of Mathematics, December 1969.

5. J. F. McNamara, Incremental Stiffness Method for Finite Element Analysis of the Nonlinear Dynamic Problem, Ph.D. Thesis, Brown University, June 1972.

MARC-CDC is a non-linear general-purpose program which attempts to incorporate the latest in finite-element technology. The program consists of various modules, each of which represents a particular aspect of finite-element technology -- such as element geometry, material behavior, structural mechanics and matrix manipulation.

The modules may be selected and used simultaneously with each other in a variety of combinations, resulting in a broad-based program which achieves the full potential of a general-purpose program. Aimed at moderate-size problems, the program offers up to 10,000 degrees of freedom (depending on bandwidth size) and maintains a balance between efficiency and size.

Designed to operate on CDC 6600 computer systems, MARC-CDC was developed by the MARC Analysis Research Corporation of Providence, R.I. It is available in the United States through Control Data Corporation's CYBERNET services network.

PROGRAM CAPABILITIES

Because of its many capabilities, MARC-CDC is well suited for state-of-the-art analysis in applications such as pressure-vessel design, nuclear reactor design, and aerospace and automotive research. Among the many modules of MARC-CDC are the following libraries, programs, and sub-programs:

Element Library -- a library of 25 elements, including curved beams with open and closed sections in one, two and three dimensiona; plates and shells; and solid two and three-dimensional isoparametric elements. These elements, when used in combination, have been selected so they can model any conceivable structure, depending upon size limitations of the program.

A special linkage feature enables the interconnection of shell and solid elements. All elements incorporated within the total MARC-CDC library have been constructed to permit the use of large displacement behavior and non-linear material behavior theories.

Non-linear Behavior Library -- This library contains a selection of theories which cover the major material nonlinearities encountered in structural analysis. Creep analysis is effected by an initial strain procedure. Elastic-plastic analysis with either isotropic or kinematic hardening (in full nine-dimensional stress space) and temperature-dependent material properties is performed with an incremental (tangent modulus) procedure. A pressure-dependent yield stress is available for use with soil and other pressure-dependent materials (generalized Mohr-Coulomb behavior).

Structural Theory -- Program control has been implemented to permit the combination of both the element library and behavior library in a series of piece-wise linear incremental analyses of every type of structure. Accordingly, analysis problems involving creep, buckling, combined nonlinear material and geometric behavior may be performed.

Compatible Heat-Transfer Analysis -- A separate nonlinear finite-element heat transfer program generates compatible thermal data for use with the stress program. Typical problems include fusion (latent heat) effects, temperature-dependent thermal properties and nonlinear boundary conditions (such as radiation).

Pre-Processor Programs -- MARCMESH-2D and MARCMESH-3D are available for the generation and bandwidth optimation of two and three-dimensional problems. With MARCSTRUCPL, input data may be plotted in planes or perspective.

Restart and Automatic Load Incrementation -- These features have been developed during extensive experience with nonlinear analysis and result in an economy of computing time. The actual flow of an analysis can be seen by following the flow sequence given in Figure A.1.

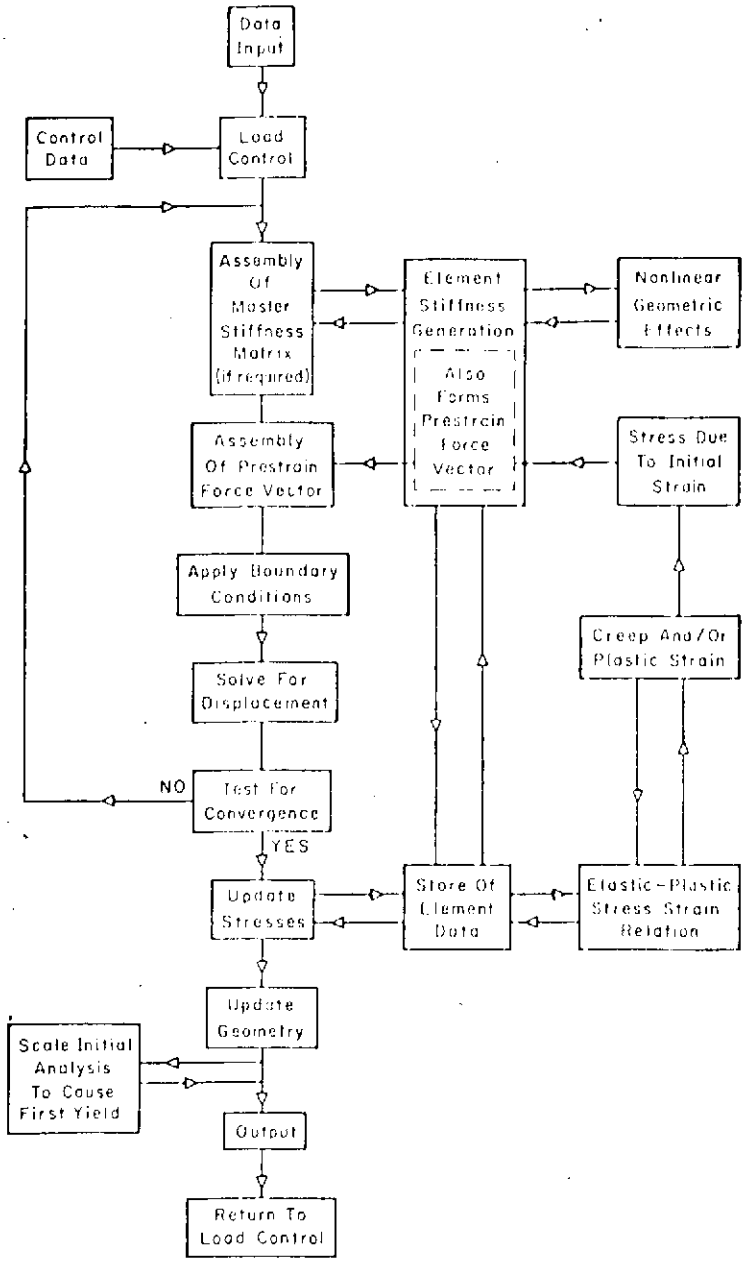

Figure A-1
Flow Chart for Computer Program

ADDITIONAL FEATURES

MARC-CDC also permits users to substitute their own subroutines to perform special tasks, thereby increasing the overall flexibility of the total program. These subroutines may cover a wide range of functions, from special input and output, to special creep laws and boundary conditions for thermal analysis. In addition, the MARC Corporation is currently developing many other modules and capabilities to further enhance the program.

PROGRAM CAPABILITIES USED IN PROJECT

CURVED TRIANGULAR SHELL ELEMENT -

MARC-CDC Element 8

Because we are concerned with the use of the curved triangular shell element - Element 8, we shall give a brief description of this element and its major features. This element is an isoparametric curved triangular shell element based on the Koiter-Sanders shell theory, which fulfills continuity requirements and represents rigid-body motions exactly.

GEOMETRY

The middle surface of the shell is defined by the equations:

$$x = x(\theta_1, \theta_2)$$

$$y = y(\theta_1, \theta_2)$$

where

(x, y, z) are Cartesian coordinates.

(θ_1, θ_2) denote Gaussian coordinates on the middle surface of the shell

The domain of definition in the plane (θ_1, θ_2) is divided into a mesh of triangles which are mapped onto curved elements on the middle surface Σ. The actual middle surface is approximated by a smooth surface $\bar{\Sigma}$ which has the same coordinates (x-y-z) and the same tangent plane at each nodal point of the mesh. Practically, the mesh is defined by the Gaussian coordinates $(\theta_{1i}, \theta_{2i})$ of the nodal points, and the surface Σ is defined by the values of According to the terminology of MARC-CDC, the coordinates are, therefore, the set:

$$\theta_{1i},\ \theta_{2i},\ x(p_i),\ \partial x(p_i)/\partial\theta_1,\ \partial x(p_i)/\partial\theta_2$$

$$y(p_i),\ \partial y(p_i)/\partial\theta_1,\ \partial_y(p_i)/\partial\theta_2$$

$$z(p_i),\ \partial z(p_i)/\partial\theta_1,\ \partial z(p_i)/\partial\theta_2$$

where

$x(p_i)$ stands for $x(\theta_{1i}, \theta_{2i})$, $(\theta_{1i}, \theta_{2i})$ being the coordinates of the node p_i.

DISPLACEMENTS

There are nine degress of freedom for each nodal point p_i. These degrees of freedom are defined in terms of the Cartesian components of displacement u,v, and w, and rates of change with respect to the Gaussian coordinates.

$$u(p_i),\ \partial u(p_i)/\partial\theta_1,\ \partial u(p_i)/\partial\theta_2$$

$$\underline{U}_i$$

$$v(p_i),\ \partial v(p_i)/\partial\theta_1,\ \partial v(p_i)/\partial\theta_2$$

$$\underline{V}_i$$

$$w(p_i),\ \partial w(p_i)/\partial\theta_1,\ \partial w(p_i)/\partial\theta_2$$

$$\underline{W}_i$$

The displacements within an element are defined by interpolation functions. These interpolation functions $\phi(\theta_1, \theta_2)$ are such that compatibility of displacements and their first derivatives is insured between adjacent elements. Hence, for an element whose vertices are the nodal points p_i, p_j and p_k, the components u, v, w are defined as:

$$u(\theta_1, \theta_2) = (\underline{U}_i^T, \underline{U}_j^T, \underline{U}_k^T) \cdot \phi(\theta_1, \theta_2)$$

$$v(\theta_1, \theta_2) = (\underline{V}_i^T, \underline{V}_j^T, \underline{V}_k^T) \cdot \phi(\theta_1, \theta_2)$$

$$w(\theta_1, \theta_2) = (\underline{W}_i^T, \underline{W}_j^T, \underline{W}_k^T) \cdot \phi(\theta_1, \theta_2)$$

NUMERICAL INTEGRATION

For this element, seven points of integration are used, with a rule which is exact for all polynomials up to the fifth order.

LOADS

Three different distributed loads are possible. The first case is a uniform load proportional to the surface area, positive when applied in the negative z-direction. The second case is a uniform normal pressure per unit of area on the surface. The third case is a non-uniform normal pressure per

unit surface area. In addition to uniform loads, concentrated loads may be applied at the nodes.

LARGE DEFORMATION ANALYSIS

The large deformation analysis follows the Lagrangian description used in MARC-CDC [A1]. Note that only large deflection terms corresponding to the stretching strains have been introduced. This approximation is usually acceptable even for nonlinear buckling analysis.

CURVED QUADRILATERAL THIN-SHELL ELEMENT - ELEMENT 4

This is an isoparametric, doubly-curved thin shell element, using bi-cubic interpolation functions. The element is based on Koiter-Sanders shell theory, fulfilling continuity requirements, and represents rigid body modes exactly when used as a rectangle in the mapped surface coordinate plane. The element contains no patching functions, so that it is restricted to quadrilateral meshes with a maximum of four elements sharing one common node. However, the element is rapidly convergent in most problems which allow such a mesh. Note that any suitable surface coordinate systems may be chosen, so that the mesh need not be rectangular on the actual surface.

GEOMETRY

The element is isoparametric, so that the actual surface is interpolated from nodal coordinates. The mesh is defined in the θ^1-θ^2 plane of surface coordinates. Then the actual surface is approximated by a surface defined by cubic interpolation on the interior of each element based on the following set of 14 nodal coordinates:

$$\theta^1,\ \theta^2,\ x,\ \frac{\partial x}{\partial \theta^1},\ \frac{\partial x}{\partial \theta^2},\ y,\ \frac{\partial y}{\partial \theta^1},\ \frac{\partial y}{\partial \theta^2},\ z,\ \frac{\partial z}{\partial \theta^1},\ \frac{\partial z}{\partial \theta^2},\ \frac{\partial^2 x}{\partial \theta^1\ \partial \theta^2};\ \frac{\partial^2 y}{\partial \theta^1\ \partial \theta^2},\ \frac{\partial^2 z}{\partial \theta^1\ \partial \theta^2}$$

In most practical cases, the surface is definable as:

$$x = x(\theta^1, \theta^2)$$
$$y = y(\theta^1, \theta^2)$$
$$z = z(\theta^1, \theta^2)$$

Then the usual procedure is to define the mesh in the θ^1-θ^2plane (as a rectangular mesh) by supplying the first two coordinates, θ^1, θ^2, at each node, through the COORDINATE input option. Then the remaining 12 coordinates are defined at each node through the use of the subroutine FXORD.

The thickness of the element is defined in EGEOM1. Note that when elements of differing thickness abut, tying must be used to avoid the imposition of improper continuity of membrane strain.

DISPLACEMENT

There are 12 degrees of freedom at each node: these are

$$u, \frac{\partial u}{\partial \theta^1}, \frac{\partial u}{\partial \theta^2}, v, \frac{\partial v}{\partial \theta^1}, \frac{\partial v}{\partial \theta^2}, w, \frac{\partial w}{\partial \theta^1}, \frac{\partial w}{\partial \theta^2}, \frac{\partial^2 u}{\partial \theta^1 \partial \theta^2}, \frac{\partial^2 v}{\partial \theta^1 \partial \theta^2}, \frac{\partial^2 w}{\partial \theta^1 \partial \theta^2}$$

where u, v, w are the Cartesian components of displacement.

Displacement is interpolated by complete bi-cubic on the interior of an element, so that equality of the above nodal degrees of freedom at the coincident nodes of abutting elements ensures the necessary continuity required for thin shell theory.

Note that fixed displacement boundary conditions should never be associated with all 12 degrees of freedom at each node, since 3 degrees of freedom must always determine middle surface (membrane) strains at the node. Care must therefore be exercised both in the specification of kinematic boundary conditions-- they must be fully, but not over-fully specified, and in the application of moments so that the generalized forces and the conjugate displacement multiply together to give a rate of mechanical work.

CONNECTIVITY SPECIFICATION AND NUMERICAL INTEGRATION

The nodal point numbers of the element must be given in anti-clockwise order on the θ^1-θ^2 plane, starting with the point (min θ^1 and θ^2). Thus, in Figure A-2, the connectivity must be given as i, j, k, l.

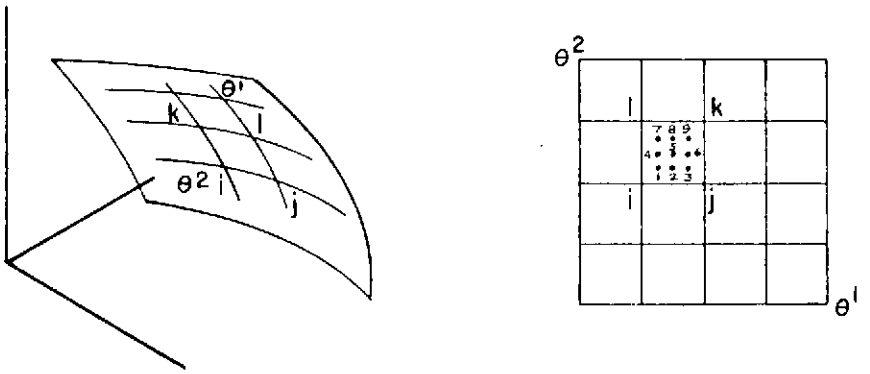

FIG. A-2 FORM OF ELEMENT 4

The element is integrated numerically using 9 points (Gaussian quadrature). The first integration point is always closest to the first node of the element, then the integration points are numbered as shown in Figure A-2. Point 5 (centroid of the element in the θ^1-θ^2 plane is used for stress output if NSTRESS=0 (or ALL POINTS option not flagged).

LOADS

Distributed Loads

Three specifications of distributed loads are available with this element. These are described below.d below.

Distributed Load Type 1

This gives a uniform load, proportional to surface area, positive in the negative z-direction (self-weight or snow load).

Distributed Load Type 2

Uniform normal pressure per unit area of surface. The magnitude of the pressure

is positive when applied in the negative $\underline{n}$ direction where $\underline{n} = \underline{a}_1 \times \underline{a}_2$ is the normal to the surface: $\underline{a}_1$ is tangent to the positive θ_1 line, $\underline{a}_2$ is tangent to the positive θ_2 line.

Distributed Load Type 3

This is a normal pressure per unit area of surface and is the same as type 2 except the magnitude is a function of position. The magnitude is defined in the user subroutine FORCEM: the required header cards are:

```
SUBROUTINE FORCEM(PRESS,TH1,TH2,NN,N)
User Coding
RETURN
END
```

with PRESS = magnitude of pressure at this point, defined by the user in this routine.

TH1, TH2 } Surface coordinates of the point, passed in for use in this routine.

NN Integration point number.

N Element number.

This subroutine will be called once per integration point in all elements of type 4 listed with load type 3. For such elements, the magnitude of load input in TRACTIONS, card series 5, will be ignored and the value defined in the user subroutine FORCEM will be used instead. Note that TH1, TH2, NN and N must not be changed.

Security Classification

DOCUMENT CONTROL DATA - R & D

(Security classification of title, body of abstract and indexing annotation must be entered when the overall report is classified)

1. ORIGINATING ACTIVITY *(Corporate author)*

Marc Analysis Research Corporation
105 Medway Street
Providence, RI 02906

2a. REPORT SECURITY CLASSIFICATION

Unclassified

2b. GROUP

N/A

3. REPORT TITLE

WATER IMPACT ANALYSIS OF SPACE SHUTTLE SOLID ROCKET MOTOR BY THE FINITE ELEMENT METHOD

4. DESCRIPTIVE NOTES *(Type of report and inclusive dates)*

Technical Report

5. AUTHOR(S) *(First name, middle initial, last name)*

Oral Buyukozturk, H. D. Hibbitt, E. P. Sorensen

6. REPORT DATE

March, 1974

7a. TOTAL NO. OF PAGES

ninety

7b. NO. OF REFS

Five

8a. CONTRACT OR GRANT NO.

NAS8-29195

b. PROJECT NO.

c.

d.

9a. ORIGINATOR'S REPORT NUMBER(S)

NAS8-29195/1

9b. OTHER REPORT NO(S) *(Any other numbers that may be assigned this report)*

10. DISTRIBUTION STATEMENT

Reproduction in whole or in part is permitted for any purpose of the United States Government.

11. SUPPLEMENTARY NOTES

12. ~~SPONSORING MILITARY ACTIVITY~~

NASA
Marshall Space Flight Center
Alabama 35812

13. ABSTRACT

A study was made of the Space Shuttle Rocket Motor Casing during water impact. The problem was assumed to be static and equivalent static loads were used. The objective was to ascertain that current finite element analysis techniques could be relied on for design purposes.

Preliminary analysis showed that the doubly curved triangular shell elements were too stiff for these shell structures. The doubly curved quadrilateral shell elements were found to give much improved results.

A total of six load cases were analyzed in this study. The load cases were either those resulting from a static test using reaction straps to simulate the drop conditions or under assumed hydrodynamic conditions resulting from a drop test. The latter hydrodynamic conditions were obtained through an emperical fit of available data.

Results obtained from a linear analysis were found to be consistent with results obtained elsewhere with NASTRAN and BOSOR.

The nonlinear analysis showed that the originally assumed loads would result in failure of the shell structures. The nonlinear analysis also showed that it was useful to apply internal pressure as a stabilizing influence on collapse.

A final analysis with an updated estimate of load conditions resulted in linear behavior up to full load.

DD FORM 1 NOV 65 1473

Security Classification

14. KEY WORDS	LINK A		LINK B		LINK C	
	ROLE	WT	ROLE	WT	ROLE	WT
Structural Analysis						
Space Shuttle Rocket Motor						
Finite Element Analysis						